Research paper

Diagenetic evolution and chemical changes of deep-water mudstones of Shahejie Formation in the Dongying Sag, Jiyang Depression, Eastern China

Tian Yang[a,b,c,*], Yingchang Cao[a,**], Henrik Friis[c], Yanzhong Wang[a], Lingli Zhou[d]

[a] School of Geosciences, China University of Petroleum, Qingdao, Shandong Province 266580, China
[b] Shandong Provincial Key Laboratory of Depositional Mineralization & Sedimentary Minerals, Shandong University of Science and Technology, Qingdao 266580, Shandong, China
[c] Department of Geoscience, Aarhus University, Høegh-Guldbergs Gade 2, DK-8000 Aarhus C, Denmark
[d] Department of Geology, Museum Building Trinity College Dublin, Dublin 2, Ireland

A B S T R A C T

The diagenetic evolution and chemical changes of mudstones have a significant influence on the reservoir quality of the mudstones and their interbedded sandstones. To investigate, a variety of methods were applied to the mudstones in the middle of the third member of the Shahejie Formation (Es3z), which were formed in a lacustrine basin during 43.7–38.2 Ma. Optical microscopy and XRD analysis show that the mudstones are dominated by clay minerals (56.8%) followed by carbonate (18.2%), quartz (14.9%), feldspar (8.4%), pyrite (0.9%), anhydrite (0.8%), and total organic carbon (TOC: 2.4%). Cementation and replacement are the main diagenetic events in the mudstone of Es3z. Carbonates and clay minerals are the most common cements, but occasionally authigenic pyrite, albite, and quartz are also present. At the eogenetic stage, the diagenetic events comprised precipitation of pyrite, siderite, dolomite, and calcite besides transformation of K-feldspar into kaolinite. During the mesogenetic stage, the main diagenetic events included precipitation of fracture-filling calcite, ferroan calcite, ankerite, microcrystalline quartz, quartz overgrowth, and transformation of K-feldspar into illite and albite. The limited variation of the Nb/Ta and Zr/Hf ratios and the almost identical distribution pattern of the REE and trace elements indicate that the detrital material in the mudstones was sourced by a common provenance of felsic igneous rocks. The CIA values of Es3z mudstones vary from 50.59 to 65.05 and the PIA values vary from 50.86 to 75.58, which confirm a low-intensity weathering of the source area. Thus, the variation in the bulk-rock geochemical composition of the mudstones may not be primary, but instead a result of mass transfer with the interbedded sandstones during diagenesis. Changes ratios between aim elements (Al, Si, Ca and K) and immobile elements with burial depth in combination with mass balance calculation indicate that aluminum and silicon were retained by the precipitation of authigenic minerals in the mudstone. The mudstones have received progressively more potassium with increasing depths, whereas calcium has been expelled. The reservoir quality of the Es3z sandstones has mainly been affected by the diagenetically induced decrease in the carbonate content in the mudstones causing carbonate cementation in the sandstones.

1. Introduction

As one of the most abundant types of sedimentary rock, mudstone has attracted increasing attention for being a potential driver of sandstone diagenesis and a main target for unconventional oil and gas production (Land et al., 1997; Schieber et al., 2000; Peltonen et al., 2009; Day-Stirrat et al., 2010; Thyberg and Jahren, 2011; Milliken et al., 2012; Milliken and Day-Stirrat, 2013; Taylor and Macquaker, 2014; Macquaker et al., 2014; McAllister et al., 2015). With the development of high-resolution microscopy techniques, great

achievements have been made in distinguishing the composition (Milliken et al., 2012, 2016; Milliken, 2014), diagenetic evolution processes (Milliken and Day-Stirrat, 2013; Taylor and Macquaker, 2014), and chemical changes (Day-Stirrat et al., 2010; Geloni et al., 2015) in mudstone. However, the petrographic characteristics and the element mobility during mudstone diagenesis are still controversial (Day-Stirrat et al., 2010; Milliken and Day-Stirrat, 2013; Bjørlykke, 2011).

The types of diagenesis in mudstone are still not clear because the complex detrital composition and the small pore size make it difficult to
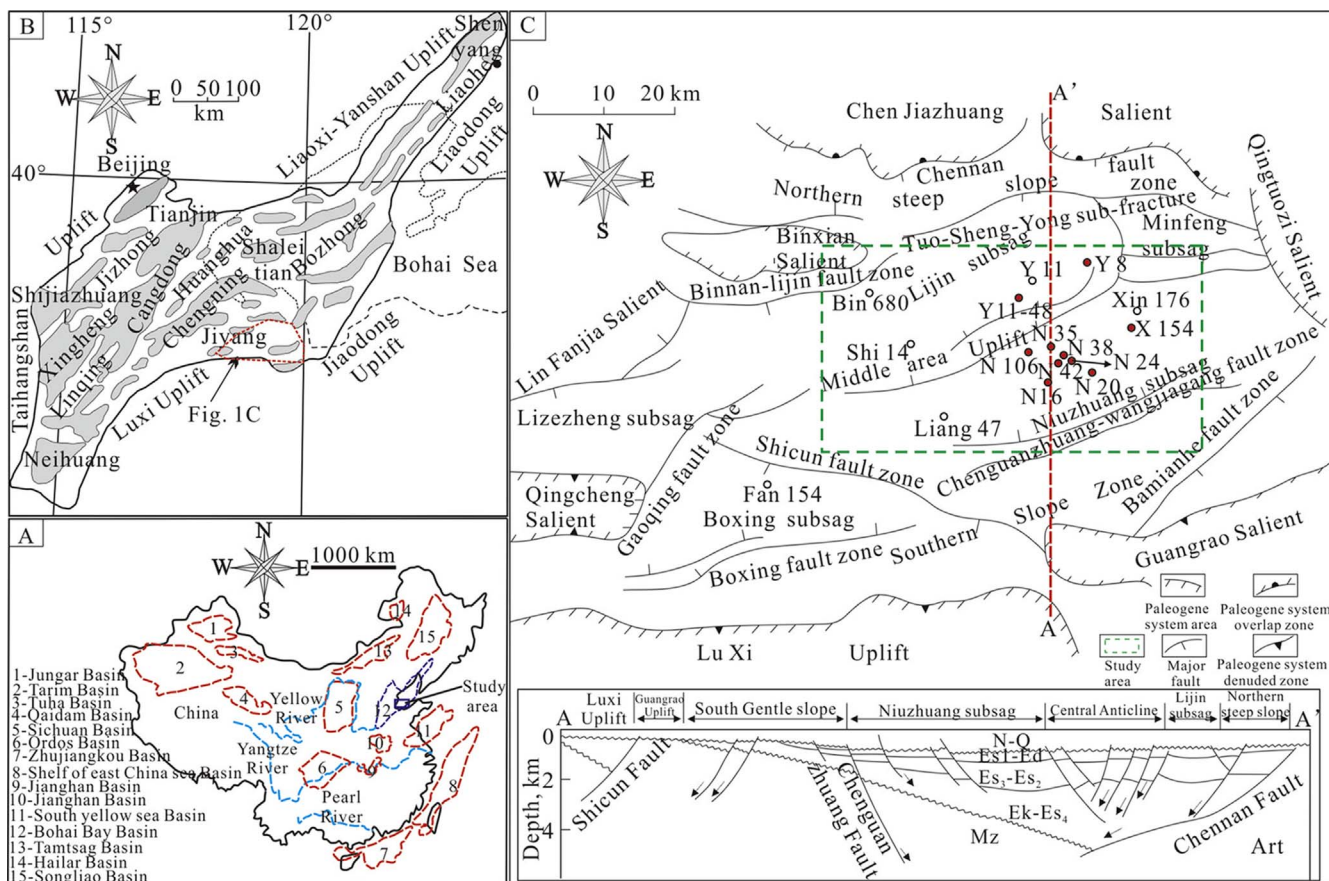
Fig. 1. (A) Location of the Bohai Bay Basin in China; (B) tectonic unit division of Bohai Bay Basin; (C) the tectonic unit division of Dongying sag and a south-to-north structural cross-section.

observe (Milliken and Day-Stirrat, 2013; Taylor and Macquaker, 2014). However, diagenesis and paragenetic sequences of mudstone are very important for understanding the changes in physical properties of unconventional reservoirs and the chemical evolution pathways (Shaw and Conybeare, 2003; Taylor and Macquaker, 2014; Dowey and Taylor, 2017). Besides, if diagenesis of mudstone acts as a source of cementation in adjacent sandstones, then the type and timing of mudstone diagenesis will be one of the dominant factors that determine the sandstone reservoir properties (Day-Stirrat et al., 2010; Geloni et al., 2015). At the same time, the effect of diagenetic reactions on the bulk composition of mudstone is not well known (Milliken and Land, 1993). Numerous studies try to understand the relationship between the petrographic and geochemical features of mudstone diagenesis (Milliken and Land, 1993; Land et al., 1997; Day-Stirrat et al., 2010; Geloni et al., 2015). Nevertheless, the effect of heterogeneity from initial compositional variation due to provenance variation cannot be avoided when using whole-rock geochemistry data (Milliken and Land, 1993; Land et al., 1997; Gier, 1998; Gier et al., 2015). The variation of provenance and geochemical weathering also affect the whole-rock elemental composition of mudstone (Milliken and Land, 1993; Land et al., 1997; Gier, 1998). Therefore, provenance and geochemical weathering analysis are important for evaluating the diagenesis and chemical changes of mudstone using whole-rock geochemistry data. Besides, research of marine mudstone has been widely reported, whereas small attention has been paid to lake mudstone in comparison (Milliken et al., 2017), which is a pity considering the differences between marine mudstones and lake mudstones (see Curtis, 1978).

The Dongying sag is a typical Mesozoic-Cenozoic lacustrine basin in the eastern part of China. There is a large volume of mudstones in the Shahejie Formation within the sag, with a thickness of approximately one thousand meters (Sui et al., 2007; Zhang et al., 2009; Hao et al.,

2014), which provides an excellent chance to study the diagenetic processes and chemical change of lake mudstone. The petrography, porosity, pore structure, and organic matter of mudstones in the third member of the Shahejie Formation, and the upper part of the fourth member of the Shahejie Formation have been investigated in detail for their high total organic carbon (TOC) content (Sui et al., 2007; Zhang et al., 2009; Hao et al., 2014). Systematic studies of the diagenetic evolution and chemical changes of the mudstone in the Dongying sag are lacking. Interbedded mudstones and sandstones are the best case study for mudstone diagenetic evolution and chemical change study (Day-Stirrat et al., 2010; Geloni et al., 2015; Gier et al., 2015). Thus, mudstones embedded within lenticular gravity-flow sandstones in the middle part of the third member of the Shahejie Formation (Es3z) are taken as an example to investigate the diagenetic evolution and chemical changes of the mudstone in the Dongying sag. The diagenesis of those lenticular gravity-flow sandstones have been investigated in Yang et al. (2017), whereas the aims of the present study are to (1) investigate the composition and types of diagenesis of the mudstones in the Es3z of the Dongying sag, (2) clarify the diagenetic evolution processes of the mudstones, and (3) evaluate the chemical changes of the mudstones constrained by provenance and geochemical weathering analysis.

2. Geological setting

The Dongying Sag is a sub-tectonic unit lying in the southeastern part of Jiyang Depression at Bohai Bay Basin, East China (Fig. 1A and B). It is a Mesozoic-Cenozoic half graben rift-downwarped basin with lacustrine facies directly deposited on Palaeozoic bedrocks (Cao et al., 2014; Wang et al., 2014) (Fig. 1C). The Dongying Sag is bounded to the east by the Qingtuozi Salient, to the south by the Luxi Uplift and
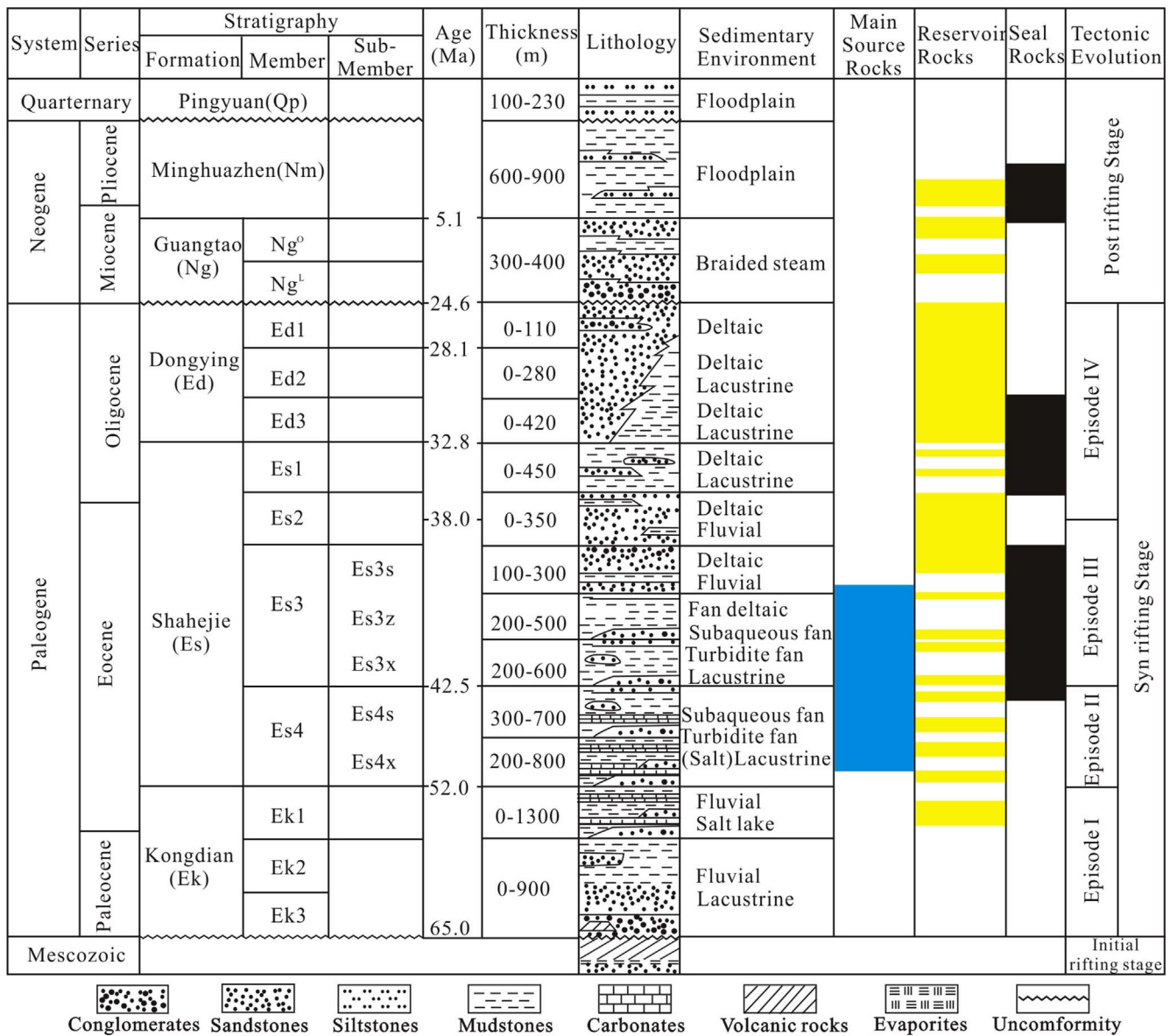
System	Series	Stratigraphy			Age (Ma)	Thickness (m)	Lithology	Sedimentary Environment	Main Source Rocks	Reservoir Rocks	Seal Rocks	Tectonic Evolution
		Formation	Member	Sub-Member								
Quaternary		Pingyuan(Qp)				100-230		Floodplain				Post rifting Stage
Neogene	Pliocene	Minghuazhen(Nm)				600-900		Floodplain				Post rifting Stage
Neogene	Miocene	Guangtao (Ng)	Ng^{O}		5.1	300-400		Braided steam				Post rifting Stage
Neogene	Miocene	Guangtao (Ng)	Ng^{L}			300-400		Braided steam				Post rifting Stage
Paleogene	Oligocene	Dongying (Ed)	Ed1		24.6 / 28.1	0-110		Deltaic				Episode IV
Paleogene	Oligocene	Dongying (Ed)	Ed2			0-280		Deltaic Lacustrine				Episode IV
Paleogene	Oligocene	Dongying (Ed)	Ed3		32.8	0-420		Deltaic Lacustrine				Episode IV
Paleogene	Eocene	Shahejie (Es)	Es1			0-450		Deltaic Lacustrine				Episode IV
Paleogene	Eocene	Shahejie (Es)	Es2		38.0	0-350		Deltaic Fluvial				Episode III
Paleogene	Eocene	Shahejie (Es)	Es3	Es3s		100-300		Deltaic Fluvial				Episode III
Paleogene	Eocene	Shahejie (Es)	Es3	Es3z		200-500		Fan deltaic Subaqueous fan				Episode III
Paleogene	Eocene	Shahejie (Es)	Es3	Es3x	42.5	200-600		Turbidite fan Lacustrine				Episode III
Paleogene	Eocene	Shahejie (Es)	Es4	Es4s		300-700		Subaqueous fan Turbidite fan				Episode II
Paleogene	Eocene	Shahejie (Es)	Es4	Es4x	52.0	200-800		(Salt)Lacustrine				Episode II
Paleogene	Paleocene	Kongdian (Ek)	Ek1			0-1300		Fluvial Salt lake				Episode I
Paleogene	Paleocene	Kongdian (Ek)	Ek2			0-900		Fluvial Lacustrine				Episode I
Paleogene	Paleocene	Kongdian (Ek)	Ek3		65.0	0-900		Fluvial Lacustrine				Episode I
Mescozoic												Initial rifting stage

Syn rifting Stage (spanning Episode I–IV)

Legend: Conglomerates · Sandstones · Siltstones · Mudstones · Carbonates · Volcanic rocks · Evaporites · Uncomformity

Fig. 2. Generalized Cenozoic stratigraphy of the Dongying Sag, showing tectonic and sedimentary evolution stages and the major petroleum system elements (After Yuan et al., 2015).

Guangrao Salient, to the west by the Linfanjia and Gaoqing Salients, and to the north by the Chenjiazhuang-Binxian Salient. The NE-trending sag covers an area of 5850 km² (Fig. 1C). It is a half-graben with a faulted northern margin and a gently sloping southern margin. Horizontally, the Dongying sag is subdivided into several secondary structural units, such as the northern steep slope zone, the middle uplift belt, the Lijin, Minfeng, Niuzhuang, Boxing subsag, and the southern gentle zone (Zhang et al., 2014).

Controlled by the tectonic activities of Tanlu fault, the Dongying sag experienced three predominant tectonic development stages: an initial rifting and subsidence in Paleocene, a syn-rift intensive rifting and subsidence in late Eocene-Oligocene, and a post-rift subsidence from the Miocene to the present (Chen et al., 2009). The strata in the sag contain Precambrian crystalline basement, Cambrian-Ordovician marine carbonates, Carboniferous-Permian terrestrial clastics and in-terbedded marine limestone, Mesozoic coarse terrestrial clastics and volcanic clastics, and Cenozoic non-marine clastics and alluvial deposits (Su et al., 2009) (Fig. 2). The Cenozoic sediments in Dongying sag consist of the Paleogene Kongdian (Ek), Shahejie (Es) and Dongying (Ed) Formations, the Neogene Guantao (Ng) and Minghuazhen (Nm) Formations, and the Quaternary Pingyuan (Qp) Formation from bottom to top (Fig. 2).

The Paleogene Shehejie Formation is the main source rock and the reservoir rock of the entire sag consisting of Es4, Es3, Es2, and Es1 from bottom to top (Fig. 2). During the deposition of Es3, the basin subsided rapidly due to intense tectonic movement and reached its maximum depth of 3600 m. Large amounts of detrital materials were consequently transported into the basin and deposited in a deep-water environment in the depressed zone and uplifted zone (Wang et al., 2013; Yang et al., 2015) (Fig. 1C). The mudstone in Shahejie Formation is an important source of oil and gas, and the thickness of each layer ranges from one centimeter to tens of meters. The diagenetic evolution of mudstone and mass transfer between the mudstone and sandstone have a significant influence on the oil generation and sandstone reservoir quality (Sui et al., 2007; Zhang et al., 2009; Hao et al., 2014).

The burial and thermal history of the sediments in Es3z of the Dongying sag were acquired by applying Basin Mod software to analyze the data from exploration wells. The present-day geothermal gradient is around 35 °C/km while the palaeo-geothermal gradient ranges from 35 to 45 °C/km (He et al., 2012). The maximum burial depth of the stratums in the Es3z in Dongying sag occurs nowadays close to 3600 m, while the average burial depth is approximately 3000 m, and the

sediments experienced a slight uplift in the early stage of Ed (Yang et al., 2017). The maximum burial temperature of the mudstones in Es3z was approximately 150 °C with a mean annual surface temperature of 15 °C (He et al., 2012). Overpressure was induced by disequilibrium stresses and hydrocarbon generation from 2200 m at around 11.4 Ma and continues today (Bao et al., 2007; Cai et al., 2009; He et al., 2012).

3. Materials and methods

X-ray diffraction (XRD) data of 67 mudstone samples, total organic carbon (TOC) contents of 87 mudstone samples, and logging data of mudstones in Es3z from 14 wells in the study area were provided by the Geological Scientific Research Institute of Sinopec Shengli Oilfield

Company. XRD clay fraction and bulk-rock compositions of 20 mudstones in Es3z were cited from Cai (2003). Besides, TOC composition of 50 mudstone samples in Es3z from Zhang et al. (2009) were compiled in this study.

3.1. Sample locations

The burial history and thermal history of sediments in the Es3z indicate that the formation temperature was approximately 120 °C at a burial depth of ∼3000 m. This temperature is favorable for a large amount of clay mineral transformation and oil generation in the mudstones of Es3z (Sui et al., 2007). Seventy-two mudstone samples were taken from 14 wells (Niu 42, Xin 154, Wangxie 543, Shishen 100, Niu 106, Niu 107, Shi 10, Shi 122, Shi 126, Shi 128, Ying 11–48, Ying 67,
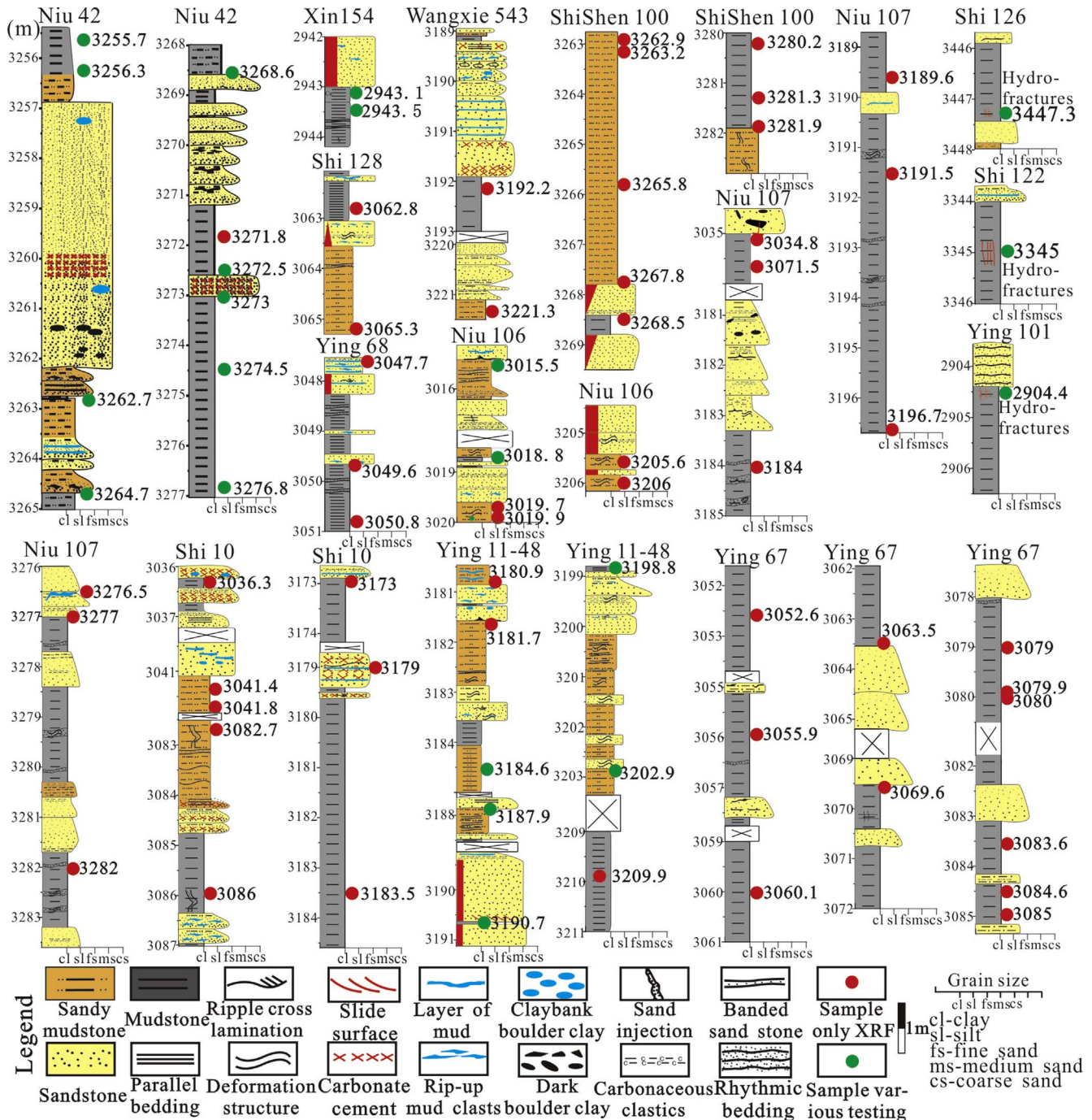
Fig. 3. Locations of the mudstone samples.

Ying 68, Ying 101) (Fig. 3), which are located in the subsag at the basin center. The burial depth of the samples are from 2700 to 3700 m.

3.2. Petrographic description

A total of 25 thin sections were prepared for mineralogy and diagenesis observations. Part of each thin section was stained with Alizarin Red S and K-ferricyanide for carbonate mineral identification with the method of Dickson (1966). Twenty-two mudstone samples were prepared for whole-rock (bulk) and clay fraction (< 2 μm) analyses by XRD using D/max-Ultima IV-ray diffractometer (Cu Kα radiation, 40 kV, 40 mA, 2°/min scanning speed, 0.0170° step width). Analysis and interpretation procedures were modified from Moore and Reynolds (1997) and Hillier (2003), with error limits of 10%. For the whole-rock analysis, samples were prepared by McCrone milling of 3 g of sample in water, followed by spray drying of the resulting slurry to obtain random powder specimens, as described by Hillier (2003). Whole-rock samples were scanned from 5.0084 to 60.9894° 2θ, counting for 2 s per 0.02 step. Clay-sized fractions (< 2 μm) were prepared by mounting the clay onto glass slides using a filter-peel-transfer method to obtain highly oriented specimens with ethylene glycol (EG)-saturated (Day-Stirrat et al., 2010). Clay fractions were scanned from 2.9950–30.0004° 2θ, counting for 1 s per 0.02 step in the air-dried state.

Twenty-two representative gold-coated sample chips were analyzed under a JSM-5500LV scanning electron microscope (SEM) (10-nA beam current, 15-kV accelerating voltage) equipped with QUANTAX 400 energy dispersive spectroscopy X-ray microanalyser (EDX) for high-resolution images and mineral identification. Semiquantitative chemical composition of minerals checking by EDX was performed by using a BRUKER Instruments Esprit 1.8 software package calibrated to the copper standard.

3.3. C-O stable isotopes, major and trace elements analyses

Twenty mudstone samples were chosen for carbon and oxygen stable isotope analyses on Thermo-Finnigan MAT 253 isotope ratio mass spectrometer. Carbon and oxygen isotope compositions of different carbonate minerals were determined by the method described by Al-Aasm et al. (1990). The bulk samples were powdered to less than 200 mesh and were then reacted with 100% phosphoric acid in vacuum at 25 °C for calcite and at 50 °C for dolomite, ankerite, and siderite (Al-Aasm et al., 1990). The reaction time for calcite, dolomite/ankerite and siderite was 1 hr, 24 hr and 3 days, respectively. The measurement precision was ± 0.08‰ for O and ± 0.06‰ for C. Carbon and oxygen stable isotope data are presented using δ notation according to the Vienna PeeDee Belemnite (V-PDB) standards.

Sixteen mudstone samples covering 4 wells were analyzed by X-ray

fluorescence spectroscopy (XRF) using a Panalytical Axios XRF Spectrometer and Thermo X-series II inductively coupled plasma source mass spectrometer (ICP-MS) at Institute of Crustal Dynamics, China, to determine the major and trace element compositions, respectively. Samples were prepared by a melting method for major elements measurements, and by a power-compressing method for trace elements measurements. In the melting method, one sample was measured from a fused disk, which was prepared at 950 °C in 5% Au–95% Pt crucibles using 0.5 g of sample, 4.5g of 12–22 Flux (lithium tetraborate-metaborate mix), and 0.0606 g of LiNO$_3$, following the method described by Robinson (2003). The results were exhibit as the weight percent of major elements, expressed as oxides (SiO$_2$, Al$_2$O$_3$, CaO, Fe$_2$O$_3$, K$_2$O, MgO, MnO, Na$_2$O, P$_2$O$_5$, and TiO$_2$). In the power-compressing method, the powdered (less than 200 mesh sieve) using a corundum ball mill; then mixed with a binder or grinding aid in a grinding vessel, with the mixture poured into a pressing die; and pressed at a pressure of 30 T. The samples were released from the form and then place in an oven at 80 °C for 1 hr. The results were exhibit as the concentration of trace elements, which are expressed in ppm (Li, Sc, V, Cr, Co, Ni, Cu, Zn, Ga, Rb, Sr, Y, Zr, Nb, Ba, La, Ce, Pr, Nd, Sm, Eu, Gd, Tb, Dy, Ho, Er, Tm, Yb, Lu, Hf, Ta, W, Pb, Th, and U). The relative standard deviation (RSD) of the measurements are less than 5% RSD of major elements and trace elements.

Another 64 samples covering 10 wells were analyzed using a Niton XL3t 950 handheld XRF instrument (40 kV mini W-Target X-Ray Tube) to determine the major and trace element compositions. Samples were slabbed and polished to reduce surface topography and then analyzed. The diameter of the round measurement area is less than 1 cm. XRF measurements were performed using a mining model to obtain the weight percent of major elements (SiO$_2$, Al$_2$O$_3$, CaO, Fe$_2$O$_3$, and K$_2$O), and using a soil model to obtain the weight percent of trace elements, expressed in ppm (Mo, Zr, Sr, U, Rb, Th, Pb, Au, Se, As, Hg, Zn, W, Cu, Ni, Co, Mn, Cr, V, Ti, Sc, S, Ba, Cs, Te, Sb, Sn, Cd, Ag, Pd, Nb, Bi, P, Cl, and Mg). The RSD of this handheld XRF ranges from 0.21% for iron (Fe) to 8.2% for cadmium (Cd) (25 mg/kg), well below 10% RSD criteria for definitive data quality.

4. Results

4.1. Petrography

Based on the bulk rock XRD data from 42 core samples (Fig. 4A) (Table 1), the content of quartz is 4.6–35.5% with an average of 14.9%. The feldspar content is 2.3–20.0% with an average of 8.4% of which K-feldspar accounts for 1.9% and plagioclase for 6.5%. The content of clay minerals ranges from 9.7 to 72.0% with an average of 56.8%. The carbonates are composed of calcite (10.0%), dolomite (0.3%), ankerite
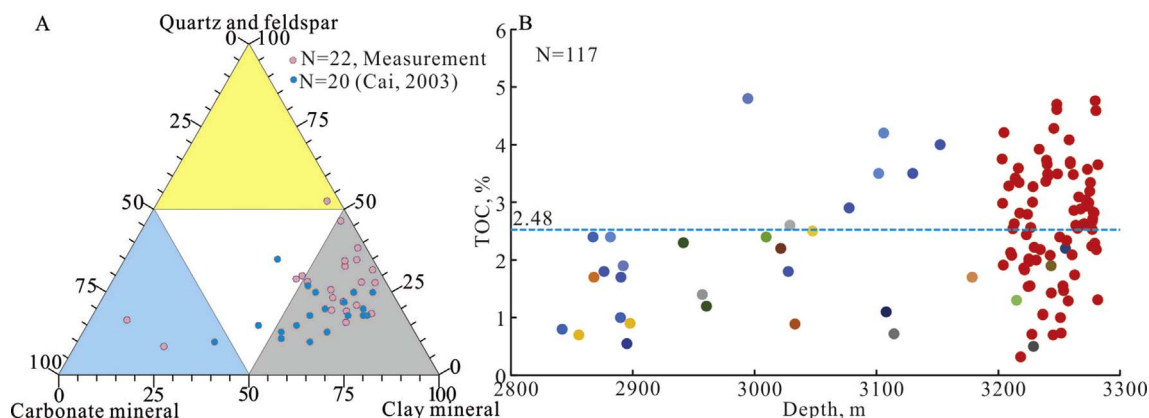

Fig. 4. Mineralogical composition of the mudstones in Es3z of Dongying sag measured by XRD analysis. (A) Classification of the mudstone according to Liang et al. (2014). Quartz and feldspar are mainly detrital but also contain minor amounts of diagenetic quartz and albite. (B) The TOC content of the mudstones (the colour indicates data from different wells). (For interpretation of the references to colour in this figure legend, the reader is referred to the web version of this article.)

Table 1
Mineralogy of mudstones measured by XRD analysis in the Es3z of the Dongying sag.

Well	Depth, m	Q	K	P	C	A	D	S	Py	An	TC	I	Ka	Ch	I/S	I/S (%I)
Xin 154	2939.4	8.4	1.7	6.5	0.0	0.0	0.0	73.7	0.0	0.0	9.7	51	15	13	21	78
Xin 154	2943.1	4.6	2.6	1.4	0.0	66.8	0.0	1.2	0.0	0.0	23.4	39	13	8	40	78
Xin 154	2943.5	16.8	1.0	1.3	17.1	0.0	0.0	0.9	2.3	0.0	60.6	37	3	3	57	55
Niu 42	3255.7	14.9	2.4	3.0	9.4	0.0	0.1	1.2	3.6	0.0	65.4	54	4	4	38	75
Niu 42	3256.3	22.1	1.1	9.2	3.8	0.0	0.0	4.3	1.5	0.0	58.0	38	16	9	37	75
Niu 42	3262.7	26.0	1.9	6.2	1.5	0.0	2.5	3.4	0.2	0.9	57.4	55	11	6	28	80
Niu 42	3263.8	35.5	4.7	11.7	1.0	0.0	0.0	2.1	0.2	1.0	43.8	39	14	8	39	80
Niu 42	3268.6	27.2	4.3	6.5	0.5	0.0	0.9	0.7	0.4	0.6	58.9	54	11	7	28	78
Niu 42	3272.5	23.8	0.9	2.2	17.6	0.0	0.7	1.2	3.3	1.3	49.0	50	5	5	40	78
Niu 42	3273.0	17.5	0.5	3.7	12.4	0.0	0.0	1.4	1.7	0.4	62.4	41	4	3	52	75
Niu 42	3274.5	16.6	0.4	1.9	11.7	0.0	0.0	2.7	1.8	0.0	64.9	55	4	4	37	75
Niu 42	3276.8	16.6	1.6	4.8	11.0	0.0	1.6	3.4	1.0	0.4	59.6	51	5	4	40	75
Ying 11-48	3181.7	24.6	0.4	3.9	19.4	0.0	0.0	0.8	3.6	0.0	47.3	58	4	4	34	80
Ying 11-48	3184.6	16.2	4.0	7.3	3.1	0.0	0.0	3.1	1.9	0.0	64.4	57	4	4	35	80
Ying 11-48	3187.9	17.2	1.3	15.8	0.0	0.0	0.0	4.1	1.0	0.5	60.1	73	9	3	15	85
Ying 11-48	3190.7	6.2	0.5	8.8	0.0	0.0	0.0	16.1	2.0	0.3	66.1	55	5	2	38	85
Ying 11-48	3198.8	18.4	2.5	10.4	0.0	0.0	0.0	1.5	1.0	0.5	65.7	52	9	4	35	85
Ying 11-48	3202.9	14.0	0.8	3.2	1.6	4.2	0.0	2.4	2.5	0.3	71.0	59	2	2	37	85
Ying 11-48	3205.0	19.4	1.4	5.9	0.0	0.0	0.0	2.7	4.2	0.0	66.4	64	2	2	32	85
Ying 11-48	3209.9	21.0	0.1	4.0	13.3	0.0	0.0	1.8	2.5	0.0	57.3	85	2	2	11	85
Niu 106	3015.5	30.4	3.7	12.3	1.3	0.0	0.8	0.4	0.3	0.0	50.8	25	16	11	48	70
Niu 106	3018.8	17.0	3.8	8.2	1.7	20.3	0.0	1.0	0.0	0.0	48.0	33	16	8	43	75
*Ying 8	2803.0	10.0	2	8.0	5.0	0.0	0.0	5.0	0.0	0.0	70.0	20	30	5.0	15	62
*Niu 38	2804.0	15.0	4	16.0	15.0	0.0	0.0	0.0	0.0	10	40.0	17	10	3.0	10	#
*Niu 38	2828.7	10.0	2	8.0	10.0	0.0	0.0	5.0	0.0	5.0	60.0	30	10	5.0	15	63
*Niu 38	2836.5	10.0	1.6	6.4	10.0	0.0	0.0	0.0	0.0	0.0	72.0	25	10	5.0	32	63
*Niu 38	2874.9	10.0	3	12.0	5.0	0.0	0.0	0.0	0.0	0.0	70.0	20	20	0.0	30	62
*Niu 38	2898.7	10.0	1.6	6.4	10.0	0.0	0.0	5.0	0.0	0.0	67.0	25	20	5.0	17	#
*Niu 38	2901.0	5.0	2	8.0	15.0	0.0	0.0	25.0	0.0	0.0	45.0	10	17	3.0	15	#
*Niu 38	2918.5	20.0	1	4.0	0.0	0.0	5.0	5.0	0.0	0.0	65.0	30	10	5.0	20	66
*Niu 38	2943.3	15.0	2	8.0	6.0	0.0	0.0	0.0	0.0	4.0	65.0	10	10	5.0	44	69
*Niu 38	3020.6	8.0	1	4.0	20.0	3.0	0.0	0.0	0.0	0.0	64.0	10	10	3.0	41	73
*Niu 38	3046.3	8.0	2	8.0	20.0	0.0	0.0	5.0	0.0	0.0	57.0	24	10.	3.0	20	#
*Niu 38	3054.0	6.0	1	4.0	25.0	5.0	0.0	6.0	0.0	0.0	53.0	38	10.	5.0	0	#
*Niu 38	3088.4	5.0	1	4.0	15.0	4.0	0.0	10.0	0.0	0.0	61.0	16	10	5.0	30	#
*Niu 38	3109.2	15.0	2.4	9.6	8.0	3.0	0.0	0.0	0.0	10	52.0	9	10	3.0	30	61
*Niu 38	3125.6	15.0	2	8.0	5.0	5.0	0.0	10.0	0.0	0.0	55.0	20	10	5.0	20	69
*Niu 38	3171.0	12.0	2	8.0	5.0	3.0	0.0	6.0	0.0	0.0	64.0	36	5	3.0	20	74
*Niu 38	3197.2	10.0	1.6	6.4	8.0	0.0	0.	3.0	0.0	0.0	71.0	20	10	1.0	40	75
*Niu 38	3221.4	10.0	1	4.0	25.0	0.0	0.0	5.0	0.0	0.0	55.0	10	5	3.0	37	78
*Niu 38	3268.0	6.0	0.8	3.2	50.0	0.0	0.0	0.0	4.0	0.0	36.0	15	0	0.0	21	#
*Niu 38	3281.6	10.0	0.6	2.4	35.0	0.0	0.0	0.0	0.0	0.0	52.0	30	0	2.0	20	67

Note: *-data from Cai (2003); Q-Quartz; K-K-Feldspar; P-Plagioclase; C-Calcite; A-Ankerite; D-Dolomite; S-Siderite; Py-Pyrite; An-Anhydrite; TC-Total clay minerals; I-Illite; Ka-Kaolinite; Ch-Chlorite; I/S-Illite/Smecite; #-no data. The unit of the content of different minerals is %.

(2.7%), and siderite (5.2%), and the total content of carbonates is 1.5–73.7% with an average of 18.2%. The content of pyrite is 0–4.2% with an average of 0.9%; the content of anhydrite is 0–10.0% with an average of 0.8%. The content of TOC shows an increased trend with burial depth, and ranges from 0.3 to 4.8% with an average of 2.4% (Fig. 4B).

4.2. Diagenetic features

4.2.1. Cementation

The bulk rock and clay fraction XRD analyses identified various types of minerals that may be authigenic including mixed-layer illite-smectite, illite, pyrite, kaolinite, quartz, albite, ankerite among others (Fig. 5). Further analyses via SEM, EDX, and optical observation revealed that carbonates and clay minerals are the most common cements in the mudstones. Moreover, authigenic pyrite, albite, and quartz were also observed.

4.2.1.1. Carbonate cements. The crystal shape and colour of carbonate cements in the stained thin sections suggest five types of carbonate minerals. The colour of siderite aggregates changes from light brown to dark brown (Fig. 6A). Isolated siderite crystals occur in irregular rhombohedra (Fig. 6B). The colour of calcite cements changes from red to pink (Fig. 6C), while the colour of ferroan calcite cements is purple (Fig. 6D). Calcite and ferroan calcite fill pore space between detrital grains with irregular shapes (Fig. 6C and D). The colour of ankerite cements is blue in the stained thin sections (Fig. 6E), while dolomite cement is unstained and shows in high white under crossed polarized light (Fig. 6F). The dolomite and ankerite are characterized by typical intergranular euhedral rhombohedra crystals (Fig. 6E and F).

Calcite and ankerite are the main carbonate cements in the mudstone of Es3z (Fig. 7). Except for the pore space between detrital grains in mudstones filled by irregular calcite (Fig. 6C), regular grain, spherical, lentoid and fracture-filling calcites were also observed (Fig. 7A–F). The granular calcite is distributed along the boundary between micritic carbonates and large detrital grains, with its size changing from 5 to 10 μm (Fig. 7A). The spherical calcite is restricted to organic-rich mudstones, and has its size ranging from 10 to 30 μm (Fig. 7B and C). The lentoid calcite is relatively large and the crystal aggregates range from 20 to 80 μm in size (Fig. 7D and E). The shape of individual crystal in the lentoid calcites aggregates is rhombohedral, and clay minerals fill in the space between the individual crystals (Fig. 7E). The fracture-filling calcite with width approximately 350 μm can be subdivided into three stages according to the crystal shapes (Fig. 7F). The first stage calcite occurs as micritic linings along the fracture margins in a width of ~25 μm. The second stage calcite is
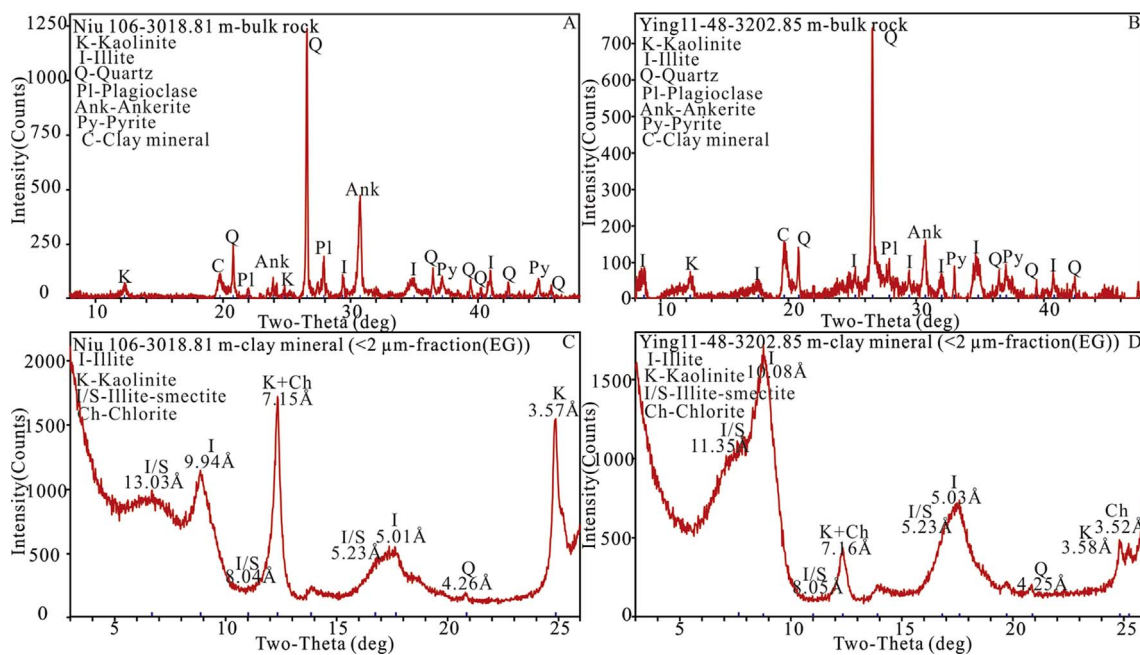
Fig. 5. Mineralogical composition of the mudstone measured by XRD analysis. (A) Niu 106, 3018.81 m-bulk rock. (B) Ying 11–48, 3202.85 m-bulk rock. (C) Niu 106, 3018.81 m-clay minerals (Oriented, ethylene glycol (EG)-saturated). (D). Ying 11–48, 3202.85 m-clay minerals (Oriented, ethylene glycol (EG)-saturated).

composed of small radial crystal in fractures of ~50 μm in width. The third stage calcite is large poikilotopic occurring in fractures of a width of ~100 μm. Bitumen coating was observed at the boundary of calcite crystals in the second and third stages of fracture-filling calcites (Fig. 7F).

Ankerite typically occurs as intergranular euhedral rhombohedra, with crystal size ranging from 5 to 15 μm (Fig. 7G and H). Ankerite crystals are in a parallel arrangement and the orientation is parallel to those of associated organic matter and clay minerals (Fig. 7G and H). The occurrence of ankerite in a radial fabric was observed when it had

formed on mica grains (Fig. 7I).

4.2.1.2. Pyrite. Framboidal pyrite (spherical aggregates of micron-sized pyrite crystals) is the most common diagenetic pyrite in the mudstones (Fig. 8A, B, and C). Individual framboids range from 1 to 30 μm in size (Fig. 8A). Tetragonal trioctahedron pyrite crystals were observed under SEM (Fig. 8B and C). The framboidal pyrite is often associated with organic matter, and concentrated in fine-grained laminae with abundant organic matter (Fig. 8A and C).
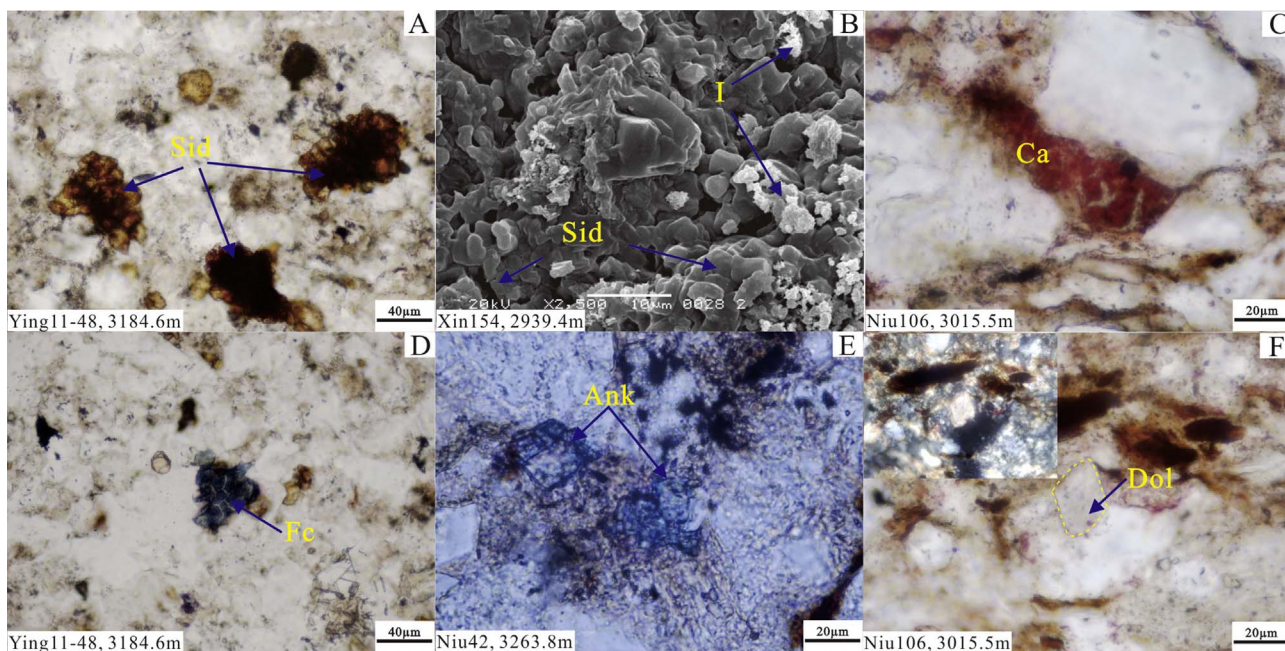
Fig. 6. Variations of carbonate cements in the mudstones of Es3z in Dongying sag. (A) Optical photomicrograph showing irregular siderite aggregations in brown colour (plane-polarized light). (B) SEM image showing siderite grains in irregular rhombohedra. (C) Optical photomicrograph showing irregular red calcite (plane-polarized light). (D) Optical photomicrograph showing irregular purple ferroan calcite (plane-polarized light). (E) Optical photomicrograph showing euhedral blue ankerite (plane-polarized light). (F) Optical photomicrographs showing euhedral dolomite (plane and crossed polarized light). Sid-Siderite, I-Illite, Ca-Calcite, Fc-Ferroan calcite, Dol-Dolomite, Ank-Ankerite. (For interpretation of the references to colour in this figure legend, the reader is referred to the web version of this article.)
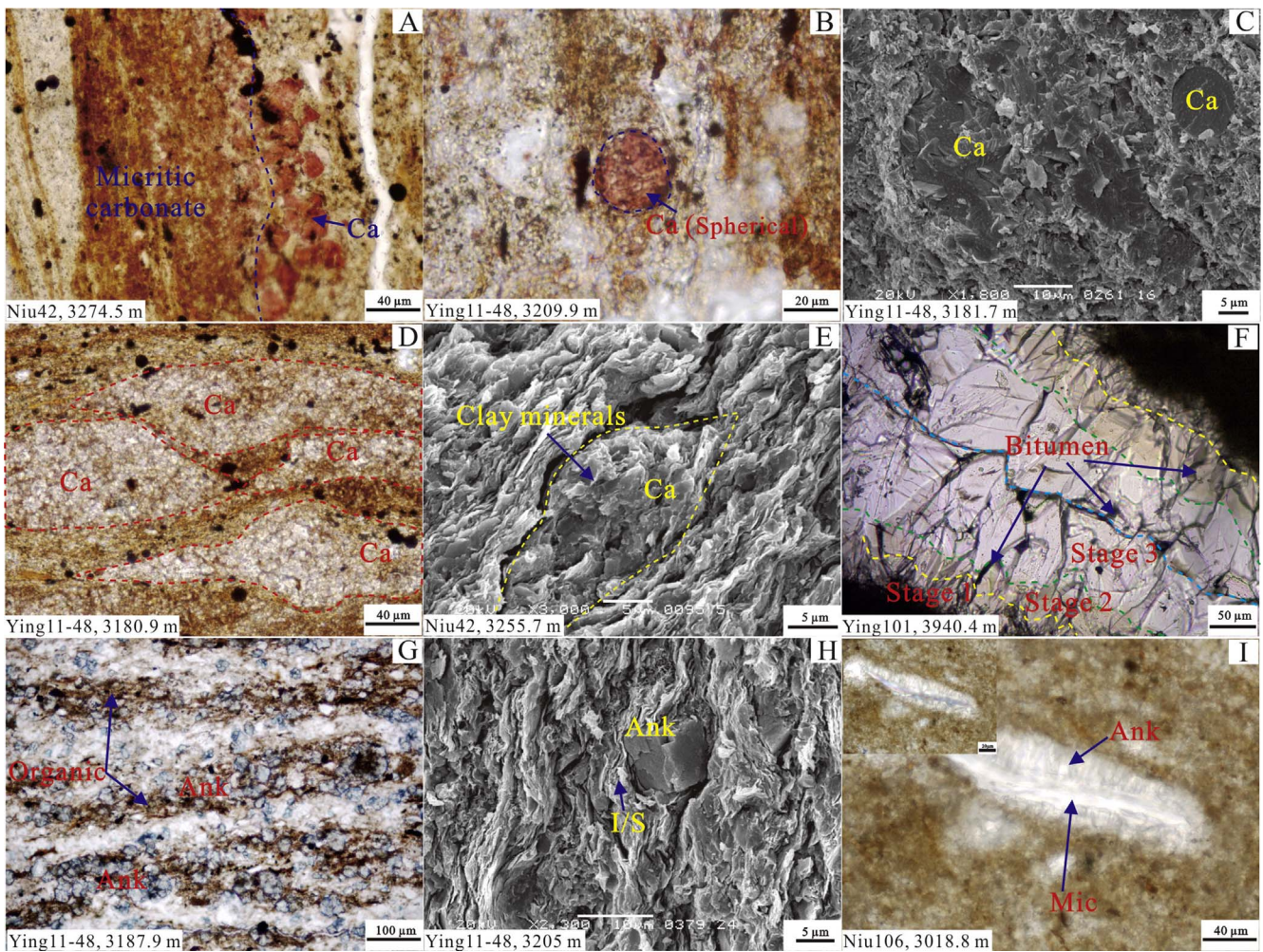
Fig. 7. Distribution of carbonate cements in the mudstone of Es3z in Dongying sag. (A) Optical photomicrograph showing irregular calcite grains (plane-polarized light). (B) Optical photomicrograph showing spherical calcite (plane-polarized light). (C) SEM image showing spherical calcite. (D) Optical photomicrograph showing lentoid calcites in grain aggregation. (E) SEM image showing lentoid calcite grain aggregation with clay minerals. (F) Optical photomicrograph showing fracture-filling calcite of three different stages of growth (plane-polarized light). (G) Optical photomicrograph showing parallel orientation arrangement ankerite (plane and crossed polarized light). (H) SEM image showing ankerite as euhedral rhombohedra surrounded by I/S. (I) Optical photomicrographs showing radial pattern ankerite (plane and crossed polarized light). Ca-Calcite, Ank-Ankerite, I/S-Illite and smectite mixed layer minerals, Mic-Mica.

4.2.1.3. Authigenic quartz. Two types of authigenic quartz can be observed in the studied mudstone samples (Fig. 8D and E). One type is quartz overgrowth on detrital grains. Quartz overgrowth is common on relatively large-sized detrital quartz grains when pore spaces was available (Fig. 8D). The euhedral terminations and edges of quartz overgrowths are regular, and the dust boundary between the detrital grain and authigenic quartz is clear under both plane-polarized light and crossed polarized light (Fig. 8D). The other type is microcrystalline authigenic quartz that fills the pore spaces between detrital grains (Fig. 8E). The size of microcrystalline quartz ranges from 5 to 15 μm (Fig. 8E).

4.2.1.4. Authigenic albite. Authigenic albite was occasionally observed in the studied mudstone samples. The lath-shaped authigenic albite crystals occur in secondary porosity from the dissolution of K-feldspar, and have an orientation parallel with the cleavage of the partly dissolved K-feldspar (Fig. 8F). Illite is closely associated with the occurrence of authigenic albite. The size of albite crystals ranges from 5 to 15 μm (Fig. 8F).

4.2.1.5. Clay minerals. According to clay fraction (< 2 μm) XRD analysis, the clay matrix mainly comprises illite and mixed-layer illite-smectite minerals with occasional kaolinite and chlorite. The crystal shape of the clay minerals observed by SEM suggests that part of the kaolinite, illite and illite-smectite mixed-layer minerals are authigenic (Fig. 9). Authigenic kaolinite with a well-developed vermiform habit usually occurs as an aggregation. Pseudohexagonal morphology of individual kaolinite crystals was observed (Fig. 9A). Part of the margin of kaolinite crystals is fibrous as a result of illitization (Fig. 9A). Authigenic illite occurs as fibrous and lath-like crystals (Fig. 9B and C). Fibrous illite is commonly associated with kaolinite, albite and dissolved K-feldspar (Fig. 9B), while lath-like illite crystals fill the space between detrital grains (Fig. 9C). The shape of illite-smectite mixed layer minerals varies with the contents of illite according to the XRD data and SEM observations. With a relatively low content of illite, the mixed-layer minerals occur as schistose crystals with curly margin and range from 5 to 10 μm in size (Fig. 9D). As the content of illite increases, the mixed-layer minerals occur as large schistose crystals of uniform shape, and range from 5 to 15 μm in size (Fig. 9E and F).

4.2.2. Replacement

Calcite replacement of detrital grains, kaolinization of feldspars, and albitization of feldspars are common in the studied mudstone samples (Fig. 10). The replacement of detrital grains initiated at the margin, and was most commonly by poikilotopic calcite (Fig. 10A and B). Some of
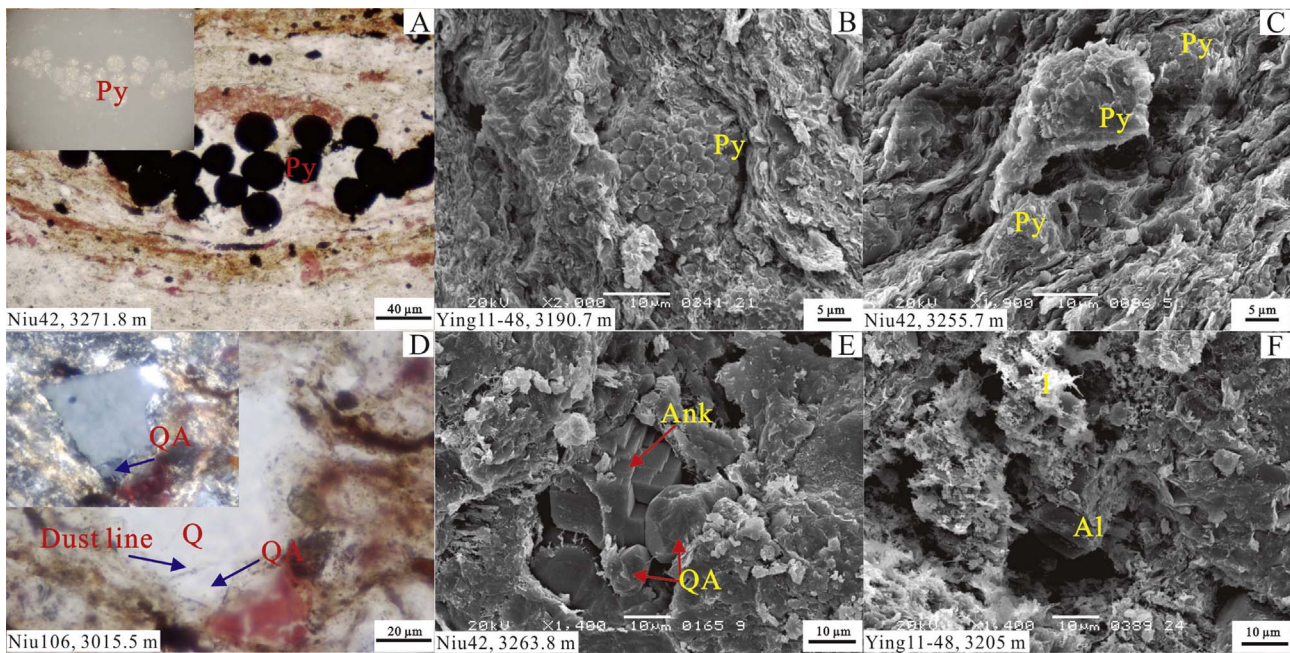
Fig. 8. Pyrite, authigenic quartz, and albite in the mudstones of Es3z in Dongying sag. (A) Optical photomicrographs showing framboidal pyrite (plane polarized light and reflected light). (B) SEM image showing framboidal pyrite and tetragonal trisoctahedron pyrite crystal. (C) SEM image showing parallel orientated pyrite. (D) Optical photomicrographs showing quartz overgrowth (plane and crossed polarized light). (E) SEM image showing microcrystalline authigenic quartzes associated with ankerite. (F) SEM image showing lath-shaped albite crystals associated with illite. Py-Pyrite, Q-Quartz, QA-Authigenic quartz, Ank-Ankerite, Al-Albite, I-Illite.
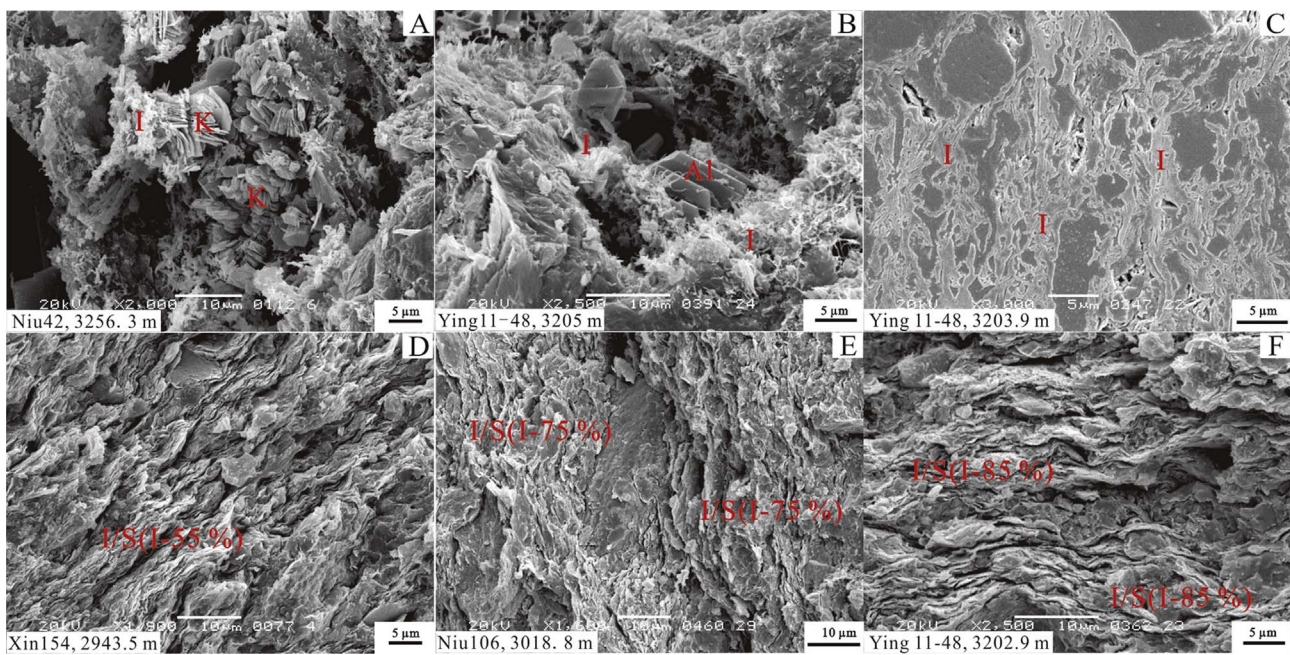
Fig. 9. Clay minerals in the mudstone of Es3z in Dongying sag. (A) SEM image showing vermiform kaolinite, part of them have undergone illitization. (B) SEM image showing fibrous illites associated with albite. (C) SEM image showing lath-like illites filling spaces between detrital grains. (D) SEM image showing schistose crystals mixed layer minerals, with curly margin. (E) SEM image showing bigger schistose crystals mixed layer minerals. (F) SEM image showing uniform schistose crystals mixed layer minerals. I-Illite, K-Kaolinite, Al-Albite, I/S-Illite and smectite mixed layer minerals.

the detrital grains are thoroughly replaced by calcite (Fig. 10C). The original shape of detrital grains can easily be observed, and in many cases, irregular remnants of the detrital grains can be observed (Fig. 10B and C). Both calcitization and kaolinization can take place on the same detrital grain (Fig. 10D). Albitization of K-feldspar and replacement by clay minerals with irregular K-feldspar remnants were observed (Fig. 10E and F). Some K-feldspar grains were totally transformed into clay minerals (Fig. 10G, H and I). The clay minerals are mainly aggregations of euhedral kaolinite that keep the shape of the

replaced detrital grain (Fig. 10G and H), and part of the kaolinites may have been transformed into illite (Fig. 10I).

4.3. Mineralogical depth trends

The bulk rock composition of the clay-dominated mudstones at various depths analysed by XRD is shown in Fig. 11. The quartz content is 13% on average when the burial depth is less than 3000 m. With increasing burial depth from 3000 to 3300 m, the quartz content
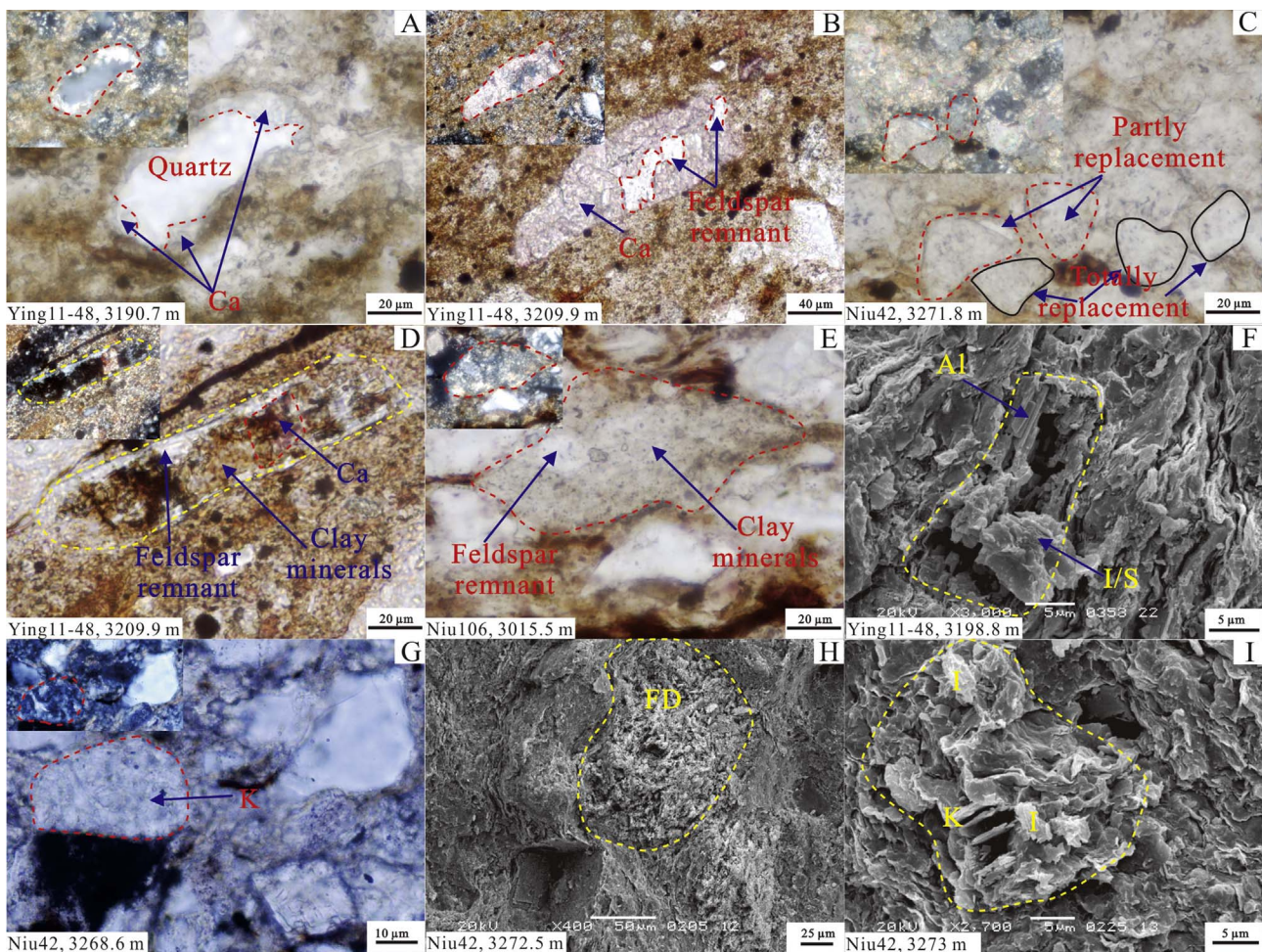
Fig. 10. Replacement of detrital grains in the mudstone of Es3z in Dongying sag. (A) Optical photomicrographs showing the margin of quartz was replaced by calcite (plane and crossed polarized light). (B) Optical photomicrographs showing feldspar was replaced by calcite from the margin to center (plane and crossed polarized light). (C) Optical photomicrographs showing partial and total calcitization of detrital grains (plane and crossed polarized light). (D) Optical photomicrographs showing calcitization and kaolinization on the same feldspar grain (plane and crossed polarized light). (E) Optical photomicrographs showing partial kaolinization of feldspar (plane and crossed polarized light). (F) SEM image showing partial albitization of feldspar. (G) Optical photomicrographs showing total kaolinization of feldspar (plane and crossed polarized light). (H) SEM image showing total kaolinization of feldspar. (I) SEM image showing total kaolinization of feldspar, with part of the kaolinite transformed into illite. Ca-Calcite, Al-Albite, I/S-Illite and smectite mixed layer minerals, K-Kaolinite, FD-Detrital feldspar, I-Illite.

increases slightly from 13.0 to 14.6% on average (Fig. 11). In the same interval, the K-feldspar content decreases from 2.0 to 1.5% while the plagioclase content decreases from 7.8 to 6.0% (Fig. 11). The content of carbonate minerals has a complex trend with burial depth. There is a clear increase in the content of carbonate minerals from 2800 to 3050 m followed by a decrease when deeper burial (Fig. 11). The content of carbonate minerals is 13.7% on average when the burial depth is less than 3050 m, and 14.2% on average when the burial depth is more than 3050 m. The clay minerals show a relatively consistent content of ca. 60%.

Mixed-layer illite-smectite minerals are the dominant clay minerals in the studied mudstone samples, and the content of all the clay minerals increases with increasing burial depth (Fig. 12). Kaolinite is most abundant at burial depths less than 2950 m with a content of 16.9% on average, and it decreases rapidly to a content of 7.8% on average at a deeper depth. The content of illite-smectite mixed-layer minerals decreases rapidly below 3000 m from 56.9 to 52.8% on average. On the contrary, the content of illite increases abruptly below 3000 m from 27.5 to 35.5% on average. The content of chlorite shows a slight increase in mudstone below 3000 m. Illite-smectite mixed layer minerals

contain less than 80% illite above 3000 m but more than 80% illite below 3000 m (Fig. 12).

4.4. Bulk-rock geochemistry

4.4.1. Major element geochemistry

According to the XRF analysis, the contents of the major elements of mudstones of Es3z in the Dongying sag are 33.50–59.88 wt. % for SiO_2, 9.01–15.55 wt. % for Al_2O_3, 1.04–14.10 wt. % for CaO, 5.87–17.65 wt. % for Fe_2O_3, 2.96–4.56 wt. % for K_2O, 1.88–4.90 wt. % for MgO, 0.03–0.30 wt. % for MnO, 1.17–2.43 wt. % for Na_2O, 0.10–0.26 wt. % for PO_5, and 0.70–2.01 wt. % for TiO_2. The weak correlation of SiO_2 vs. Al_2O_3 (Fig. 13A) suggests that the primary host of Si is quartz. Taking the low content of K-feldspar into consideration (Fig. 12), the positive correlation of K_2O with Al_2O_3 indicates that illite and smectite are the main hosts for K and Al (Fig. 13B). The positive correlation of Na_2O with SiO_2 implies that Na mostly resides in feldspar (Fig. 13C). In contrast, Al_2O_3 is negatively correlated to CaO, indicating the dominant occurrence of Ca in carbonate cements (Fig. 13D), and the two different trends of correlation of CaO vs. MgO in Fig. 13E may reflect that calcite
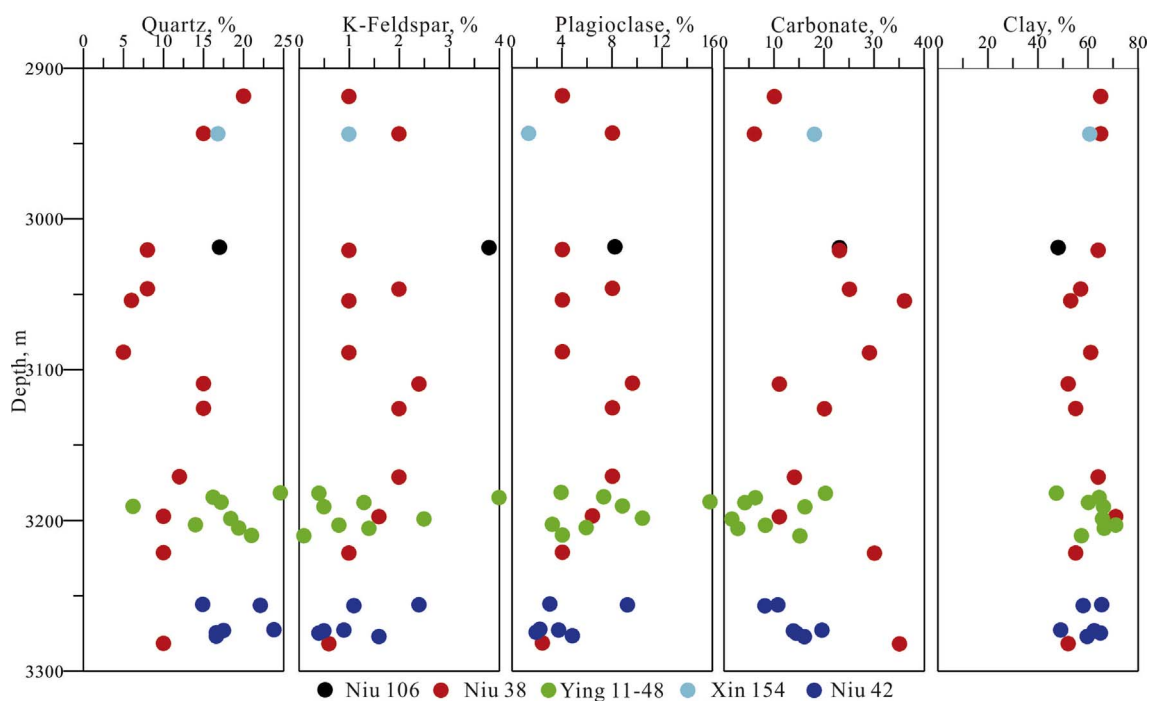
Fig. 11. XRD bulk data of mudstones in the Es3z of the Dongying sag. Only the data of the clay dominated mudstones are used.

and ankerite are the main hosting carbonates. The positive linear correlation between TiO_2 and Al_2O_3 implies that Ti is mainly associated with clay minerals (Fig. 13F).

4.4.2. Rare earth element and trace element geochemistry

The mudstone samples have negative Eu and positive Ce anomalies after being normalized to Chondrite, but vary with respect to anomaly size (Fig. 14A). The chondrite-normalized rare earth element (REE) distribution pattern for all the mudstone samples consistently show enriched LREE and flat HREE patterns (Fig. 14A). The highly

fractionated REE pattern and negative Eu anomaly indicate a felsic provenance for the mudstones of Es3z in Dongying sag, and the similarities of the REE distribution patterns among the mudstones suggest a common provenance (Fig. 14A). The ratio of HREEs to LREEs shows a slightly increasing trend from Well Xin 154 to Ying 11–48, which is most likely caused by sorting processes during transport and therefore may reflect a transport route of sediments from southeast to northwest (Figs. 1C and 14A).

Primitive mantle normalized distribution patterns of trace elements in the mudstones show various enrichment of K, Pb, Zr, and Gd, and
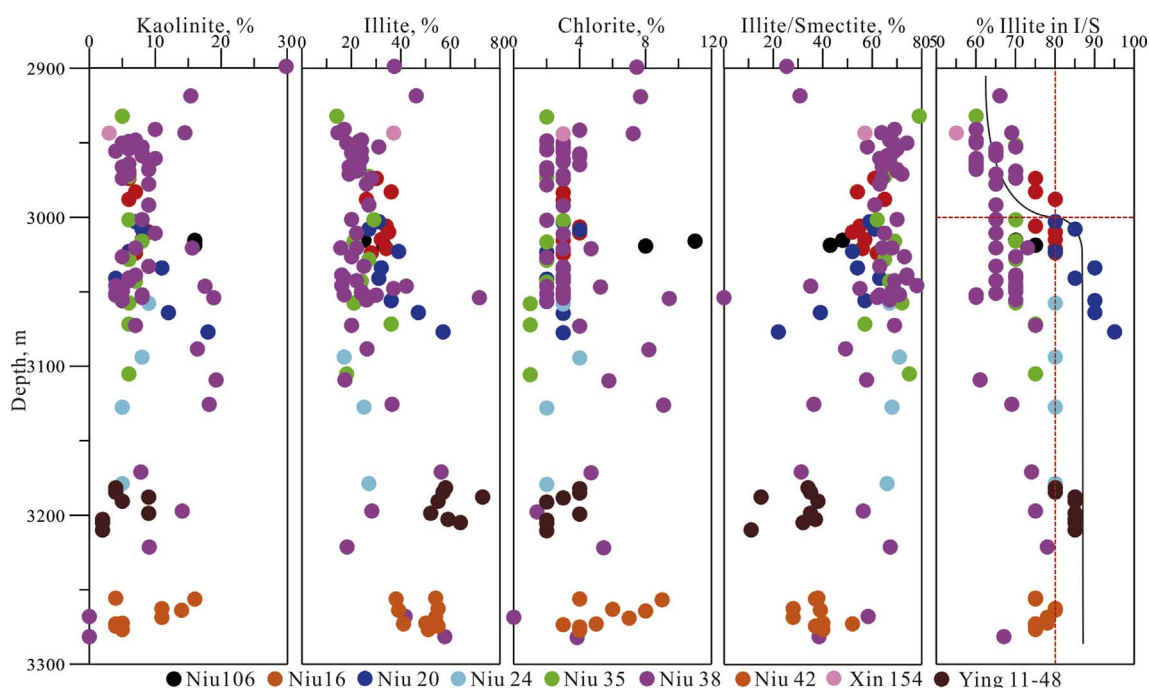
Fig. 12. XRD clay mineralogical data of the mudstones of Es3z in Dongying sag. The content of clay minerals of the other 67 samples (in Appendix 1) has been added to the data of Fig. 11 (six of the samples do not contain data on the content of illite in illite-smectite mixed-layer minerals).
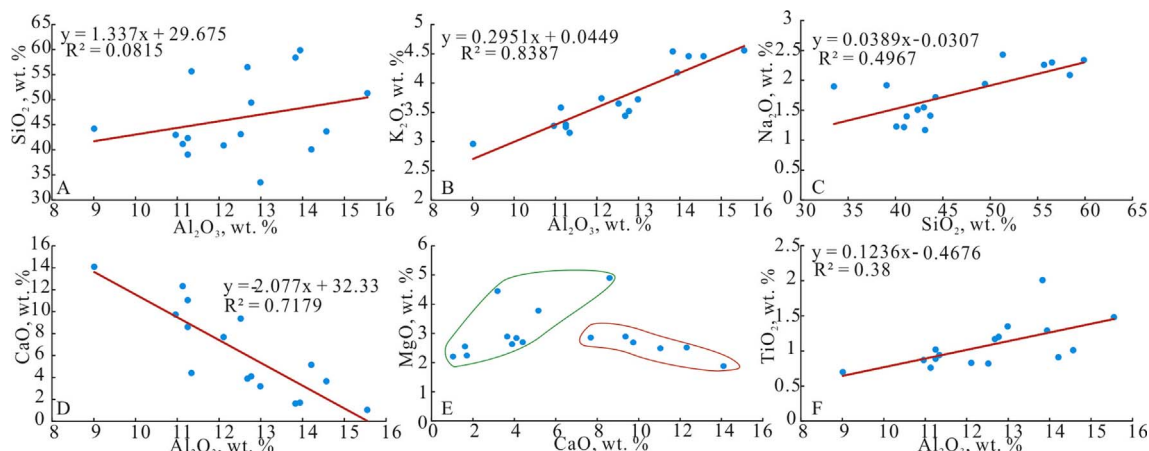
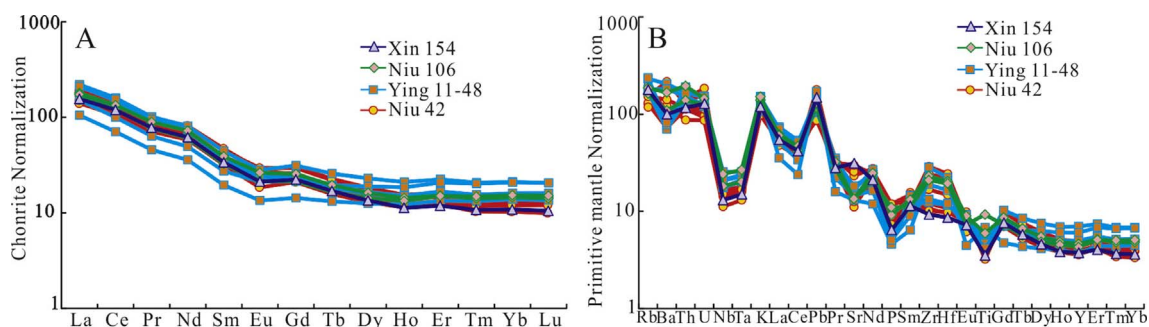Fig. 13. Major element distribution pattern of the mudstone of Es3z in Dongying sag (in Appendix 2).

Fig. 14. Rare earth element and trace element distribution of mudstones in the Es3z of the Dongying sag (in Appendix 3).

Table 2
Mineralogical and isotopic composition of carbonate cements, and calculated formation temperature of cements in Es3z of deep-water gravity-flow sandstone reservoirs. Ca-Calcite; Do-Dolomite; An-Ankerite; Fc-Ferroan calcite.

Well	Depth, m	Rock type	Carbonate minerals	Carbonate minerals content, %	$\delta^{13}C_{-PDB}$, ‰	$\delta^{18}O_{-PDB}$, ‰	Temp, °C	$^{18}O_{SMOW}$, ‰
Shi 126	3447.34	CV	100% Ca	100	4.1	−12.9	97.5	0
Shi 122	3445	CV	100% Ca	100	3.2	−12.8	96.6	0
Ying 101	2940.4	CV	100% Ca	100	0.8	−11.4	84.4	0
Xin 154	2939.4	M	100% Sid	73.4	6.9	−5.2	–	–
Xin 154	2943.1	M	98% An + 2% Sid	68	5.8	−6.3	82.8	0.25
Xin 154	2943.5	M	95% Ca + 5% Sid	18	4.2	−7.6	56.5	0
Niu 42	3255.7	M	88% Ca + 12% Sid	10.7	3.5	−8.2	60.4	0
Niu 42	3256.3	M	47% Ca + 53% Sid	8.1	3.4	−8.5	–	–
Niu 42	3262.7	M	20% Ca + 34% Dol +46% Sid	7.4	4.0	−7.6	–	–
Niu 42	3268.6	M	24% Ca + 53% Dol +33% Sid	2.1	3.9	−8.1	–	–
Niu 42	3272.5	M	90% Ca + 4% Dol +6% Sid	19.5	3.2	−10.1	74.0	0
Niu 42	3273	M	90% Ca + 10% Sid	13.8	4.5	−7.9	58.4	0
Niu 42	3274.5	M	81% Ca + 19% Sid	14.4	3.9	−8.3	61.1	0
Ying 11-48	3184.56	M	50% Ca + 50% Sid	6.2	4.3	−7.2	–	–
Ying 11-48	3187.86	M	100% Sid	4.1	5.0	−7.4	–	–
Ying 11-48	3190.65	M	100% Sid	16.1	5.4	−7.3	–	–
Ying 11-48	3198.75	M	100% Sid	1.5	3.7	−8.1	–	–
Ying 11-48	3202.85	M	20% Ca + 51% Ank +23% Sid	8.2	4.8	−7.1	–	–
Niu 106	3015.5	M	52% Ca + 32% Dol +16% Sid	2.5	1.7	−9.6	–	–
Niu 106	3018.81	M	8% Ca + 88% Ank +4% Sid	23	2.8	−9.6	108.8	0.25

Note: Only isotopic data of samples with more than 80% of one specific carbonate mineral were used to calculate the temperature. The formula used in calculating calcite mineral temperature is $1000 \ln\alpha_{calcite-water} = 2.78 \times 10^6/T^2 - 2.89$ (Friedman and O'Neil, 1977); the formula used in calculating dolomite mineral temperature is $1000 \ln\alpha_{dolomite-water} = 3.2 \times 10^6/T^2 - 1.5$ (Friedman and O'Neil, 1977), and $1000 \ln\alpha_{carbonate-water} = \delta^{18}O_{carbonate} - \delta^{18}O_{water}$.

depletion of Sr, Nb, Ta, P, and Ti (Fig. 14B). The mudstones generally show similar distribution patterns of trace elements, which confirms a common provenance (Fig. 14B).

4.5. Stable isotopic composition

The carbon and oxygen isotopic compositions of bulk mudstones

and calcite veins were analyzed. The $\delta^{13}C$ values of the calcite veins range from + 0.8 to + 4.1‰, while $\delta^{18}O$ ranges from - 12.9 to - 11.4‰. The $\delta^{13}C$ values of the mudstone range from + 1.73 to + 6.93‰, while $\delta^{18}O$ ranges from - 10.07 to - 5.20‰. Previous carbon isotope analyses of carbonate in the mudstone by Wang et al. (2008) yielded $\delta^{13}C$ ranging from - 2.47 to + 4.60‰, and $\delta^{18}O$ ranging from - 15.47 to - 8.30‰, which is similar to our results (Table 2).

5. Discussion

5.1. Diagenetic history of mudstones

The framboidal pyrites have been demonstrated to be the typical early diagenetic minerals worldwide (Taylor and Macquaker, 2000; Macquaker et al., 2014). The fresh water environment in Dongying sag resulted in a short supply of sulfate, which is a key factor for the formation of framboidal pyrite (Liu et al., 2002). The close relationship between framboidal pyrites and associated organic materials in our samples implies that these pyrites were formed from bacterial sulfate reduction of organic materials, as described by Taylor and Macquaker (2000).

Siderites and dolomites are mainly distributed around the detrital grains and occupy the primary porosity that was absent from compaction (Fig. 6A, B, and F). Dolomite occurs as regular euhedral rhombohedra in most cases, as a response to sufficient open space during growth (Fig. 6F). Moreover, the $\delta^{18}O$ value of the mudstone samples with pure siderite ranges from -8.1 to $-5.2‰$ with an average of $-7.0‰$, which is higher than the average $\delta^{18}O$ value of the mudstone samples with other kinds of carbonate cements with $-9.0‰$ (Table 2). The relatively high $\delta^{18}O$ values of siderite cemented mudstone are due to low formation temperature and imply an early precipitation (Mortimer and Coleman, 1997; Zhang et al., 2001). Therefore, both siderite and dolomite are early diagenetic products.

Given a $\delta^{18}O_{SMOW}$ value of 0‰ for pore water (Han et al., 2012; Guo et al., 2014), the calculated precipitation temperatures for calcite cement in the mudstones ranges from 56.5 to 74.0 °C (Table 2) based on the oxygen isotope fractionation factor for calcite-water (Friedman and O'Neil, 1977). The calcite mainly fills the relatively large pore spaces, which have not been diminished by compaction, suggesting its formation in an early diagenetic stage (Fig. 6C). The positive $\delta^{13}C$ values of calcite indicate fermentative degradation of organic matter as an important carbon source for these calcite cements (Mansurbeg et al., 2012; Yuan et al., 2015). Spherical calcite may be the mold of gas bubbles formed by release of methane (Zhu et al., 2014), but may also be calcite infill of calcareous fossils or organic-walled microfossils with a circular shape. However, such preserved microfossils were not observed in our sample. The lentoid calcites result from the recrystallization of micritic calcite as evidenced by the obvious clay mineral fillings in-between (Fig. 7E). Besides, the distributions of lentoid calcites are parallel to the laminae in the mudstones, which also indicates that their precursors were deposited during sedimentation (Fig. 7D).

Replacement of feldspar also occurred in the early diagenetic stage (Mansurbeg et al., 2012; Bjørlykke, 2014). The low-salinity pore water with dissolved CO_2 generated by bacterial fermentation leached the feldspar and transformed it into kaolinite while releasing silica in the early diagenetic stage (Fig. 10E, G, and H) (Dutton, 2008). The silica may not precipitate for the kinetic limit at low temperature in most situations (< 80 °C) (Worden and Morad, 2000). The very low solubility of aluminum will lead to in situ precipitation of kaolinite (Fig. 10G). The clay minerals in this stage are mainly smectite and kaolinite (Figs. 12 and 15). The content of illite-smectite mixed-layer minerals is high (30.1% on average), which indicated an origin from the detrital mud. However, a small proportion of smectite can be formed by the alteration of feldspars, micas, and pyroclastics (Şans et al., 2015), which are present in relatively low contents in the mudstones (Table 1). To summarize, the main eogenetic processes include the precipitation of pyrite, siderite, dolomite, calcite, smectite and the transformation of feldspar to kaolinite (Fig. 15).

In the mesogenetic stage, the silica released from feldspar transformation in the eogenetic stage may precipitate as overgrowths on detrital grains in the space left from compaction (Fig. 8D). The formation temperature of fracture-filling calcites ranges from 84.4 to 97.5 °C (Table 2). The occurrence of bitumen at the boundaries of calcite crystals indicates that the precipitation of calcite occurred along with the oil migration (Fig. 7F). There are two periods of hydrocarbon accumulation in the sandstones of Es3z: the first period of hydrocarbon accumulation is from 27.5 to 24.6 Ma, while the second period is from 13.8 Ma until now (Yang et al., 2016). According to the burial history (Fig. 15), the precipitation of fracture-filling calcites (84.4–97.5 °C) is from 28 to 22 Ma, which is almost contemporaneous to the first period of oil migration (Fig. 15). The different stages of fracture-filling calcites may indicate the episodic migration of oil in the mudstones (Bjørlykke, 1999).

Taking the $\delta^{18}O_{SMOW}$ value of 0.25‰ into consideration (Yang et al., 2017), the calculated precipitation temperatures for ankerite cements in the mudstones range from 82.8 to 108.8 °C (Table 2) according to the oxygen isotope fractionation factor for calcite-water and dolomite-water (Friedman and O'Neil, 1977), respectively. The association of ankerite with organic matter, mica and clay minerals indicates that the transformation of smectite to illite (Boles and Franks, 1979; McKinley et al., 2003), thermal evolution of organic matter (Land et al., 1997; Guo et al., 2014), and alteration of mica (Boles and Johnson, 1983; Claeys and Mount, 1991) possibly provided source materials for the ankerite precipitation. The ferroan calcite may have the same source material as ankerite (Boles and Franks, 1979). Moreover, association of ankerite with the microcrystalline authigenic quartz may imply that the transformation of smectite to illite also provided source materials to the ankerite formation (Fig. 8E) (Milliken et al., 1994). The XRD patterns of oriented, EG-saturated < 0.2 μm samples indicate that the transition between R1 ordered I/S and R3 ordered I/S occur between 3018.81 and 3202.85 m (Fig. 5C–D) (Moore and Reynolds, 1997; Gier, 1998). As the burial depth increases, the content of illite increases whiles the contents of the mixed-layer illite-smectite and K-feldspar decrease (Figs. 9D–F, 11 and 12). This associated processes clearly indicate that the transformation of smectite to illite consumed potassium that possibly was sourced from K-feldspar (Figs. 11 and 12). The transformation of smectite to illite released calcium, magnesium, iron, sodium, and silica. The released ions combined with CO_2, possibly from organic reactions in mudstones, lead to the precipitation of ankerite and microcrystalline authigenic quartz (Boles and Franks, 1979; Thyberg and Jahren, 2011; Dowey and Taylor, 2017).

Due to limited space available in the mudstone and a low content of detrital quartz as substrate, minor homogeneous nucleation of syntaxial quartz overgrowths were observed to occur in the mesogenetic stage. Instead, albitization and illization of feldspar are the main processes (Fig. 9B, Fig. 10E–F, and Fig. 13C). Besides transformation of smectite to illite (Fig. 9E and F), the transformation of kaolinite to illite was also common at high temperatures with an effective potassium supply, although the specific sources of potassium are not clear (Figs. 9A and 10I) (Land et al., 1997; Wilkinson et al., 2003). The clay minerals in this stage are mainly illite and illite-smectite mixed-layer minerals (Figs. 12 and 15). Sodium was released and dissolved into pore water along with potassium consumption, resulting in relatively high Na/K ratios, which enables albitization of feldspar (Aagaard et al., 1990; Bjørlykke et al., 1995). Thus, the diagenetic events in the mesodiagenetic stage include the precipitation of fracture-filling calcite, ferroan calcite, ankerite, quartz overgrowth, microcrystalline authigenic quartz, and transformation of feldspar into illite and albite (Fig. 15).

5.2. Chemical changes of mudstones

5.2.1. Geochemical provenance and weathering

The REE patterns and size of the Eu anomaly have been used to infer sources of sedimentary rocks (Condie, 1993). Felsic igneous rocks usually contain high $(La/Yb)_N$ ratios and negative Eu anomalies (Cullers, 1994). The high $(La/Yb)_N$ ratio and significant negative Eu anomaly of all the mudstone samples in the Es3z of the Dongying sag illustrate felsic igneous rocks as the source materials (Fig. 16A). For terrigenous clastic sediments, the elements with low mobility, i.e. Zr,
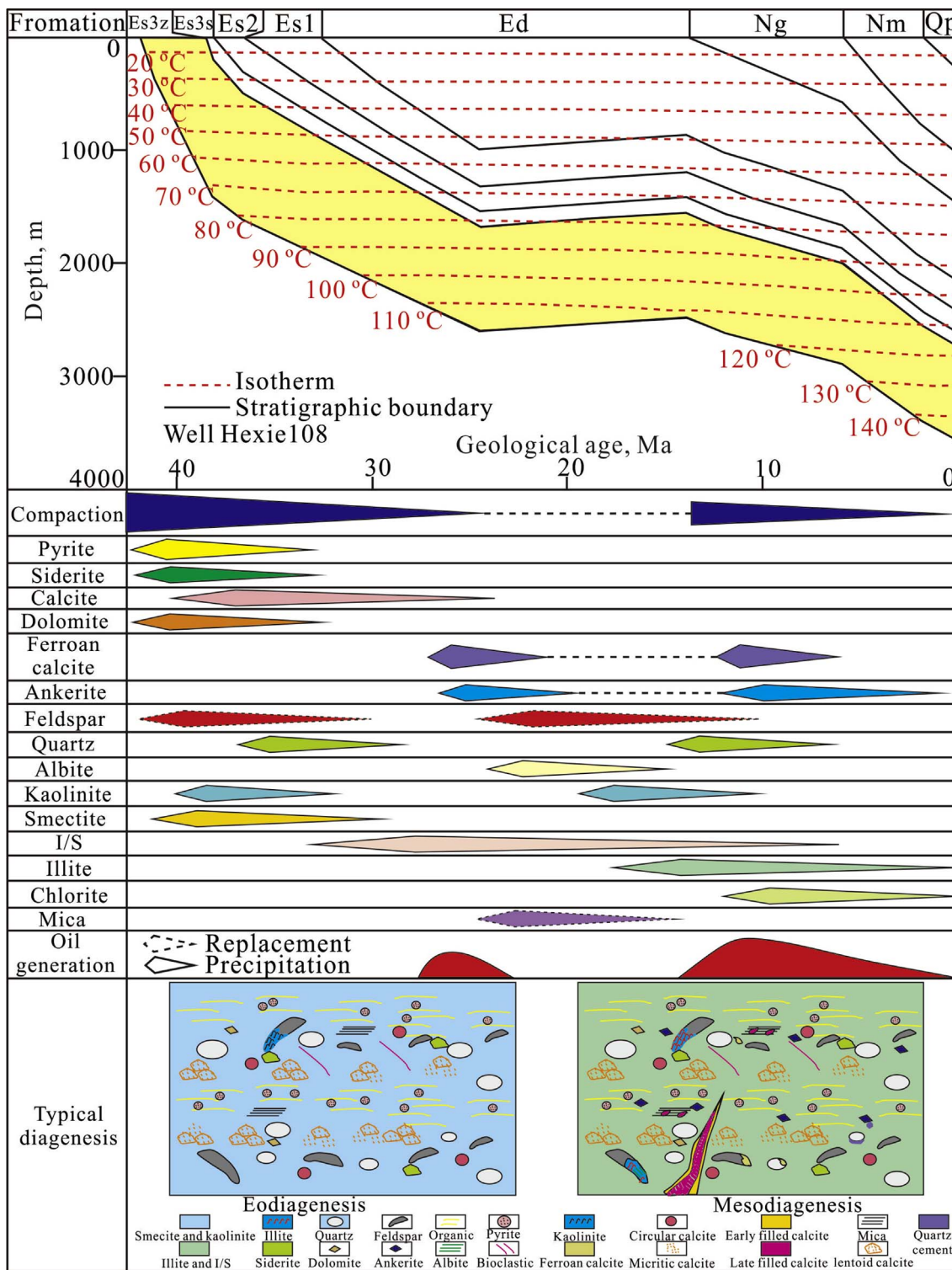
Fig. 15. Paragenetic sequence reconstructed for mudstones in the Es3z of the Dongying sag.

Hf, Ti, Nb, Ta, Cr and Sn, are preferentially hosted within stable heavy mineral phases (Preston et al., 1998). Therefore, these elemental ratios can be used as proxies for provenance-sensitive heavy mineral ratios (Cullers et al., 1988; Svendsen and Hartley, 2002). The small variation of the Nb/Ta and Zr/Hf ratios among all the mudstone samples in the Es3z of the Dongying sag indicates the same provenance of these samples (Fig. 16B). Moreover, the almost identical distribution pattern of the REE and trace elements of all the mudstone samples of Es3z in Dongying sag also implies common provenance of these samples

(Fig. 14).

The degree of chemical weathering of mudstone may have a large influence on the geochemical composition of the rocks (Vosoughi Moradi et al., 2016). To evaluate the weathering degree of the mudstone of Es3z, the Chemical Index of Alteration (CIA) (Nesbitt and Young, 1982) and the Plagioclase Index of Alteration (PIA) (Fedo et al., 1995) are taken into consideration. CIA is defined as follows: [Al_2O_3/(Al_2O_3 + CaO^* + Na_2O + K_2O)]*100 (molar proportions). Silicate-bound CaO^* is obtained, in theory, by using the equation (Fedo et al.,
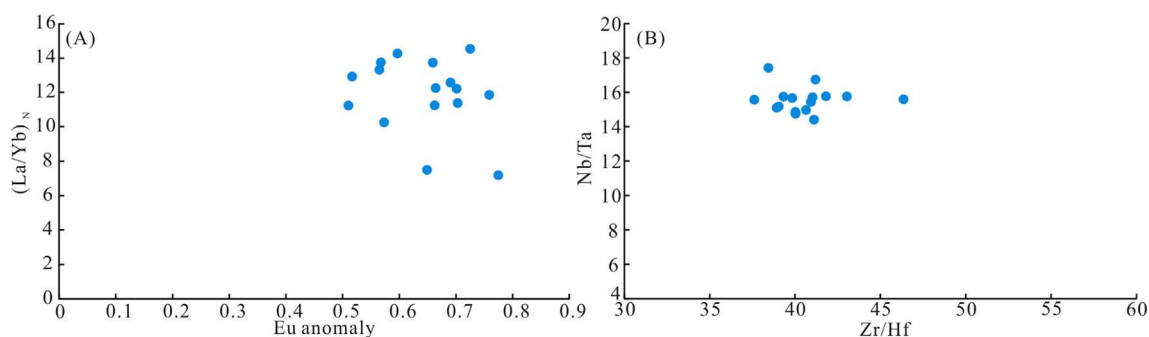
Fig. 16. Interpretation of the provenance of mudstones of Es3z in Dongying sag (in Appendix 3). (A) Binary diagram of $(La/Yb)_N$ vs. Eu anomaly; (B) Binary diagram of Nb/Ta vs. Zr/Hf.

1995): mol CaO* (silicates) = mol CaO − mol CO_2 (calcite) − 0.5 mol CO_2 (dolomite) − 10/3 mol P_2O_5. PIA is calculated by using the following equation: PIA = 100 * $(Al_2O_3-K_2O)/(Al_2O_3+CaO*+Na_2O-K_2O)$ (molar proportions). The CIA values of the mudstones in the Es3z vary from 50.59 to 65.05, the PIA values vary from 50.86 to 75.58 (Fig. 17A). The relatively lower CIA and PIA values of the mudstone samples in the Es3z confirm a low-intensity weathering of the source materials. The weathering trend can also be illustrated on A-CN-K [Al_2O_3- $(CaO* + Na_2O) − K_2O$] and A-CNK-FM [$Al_2O_3 − (CaO* + Na_2O + K_2O) − (Fe_2O_3 + MgO)$] ternary diagrams (McLennan et al., 1993; Fedo et al., 1995; Nesbitt et al., 1996; Zhou et al., 2015; Vosoughi Moradi et al., 2016; Kasi et al., 2016). There are some problems in using CaO*. Although it aims to describe the amount of silica-bound CaO which is preserved after weathering, it also depends on diagenetic changes in cases where carbonate cement is partly sourced by Ca-release from clay-mineral transformations or breakdown of other Ca-silicates. However, CaO* is useful because it eliminates the large variation in CaO content which is usually seen between samples with variable amount of carbonate cement. Our plots in the A-CN-K diagram show that the samples fall close to the feldspar line, marking a weathering trend from felsic igneous rock to some minerals between biotite and muscovite (Fig. 17B), indicating a felsic provenance. The trend is approximately parallel to IWT and away from PAAS, which indicates a weak weathering (Zhou et al., 2015). Our plots in the A-CNK-FM diagram shows that the samples close to feldspar composition imply a weak weathering, which coincides with the trend in the A-CN-K diagram (Fig. 17C).

5.2.2. Chemical changes

Since the mudstones of Es3z in Dongying sag presumably have a common provenance of felsic igneous rocks which were weakly weathered, the variation in the bulk-rock composition of the mudstones with burial depth may indicate chemical changes formed by diagenesis

(Land et al., 1997; Day-Stirrat et al., 2010). As mentioned above, there are some elements with low mobility, i.e., Zr, Hf, Ti, Nb, Ta, Cr and Sn in detrital clastic sediments, which are also called immobile elements (Preston et al., 1998; Land et al., 1997; Gluyas et al., 2000; Land and Milliken, 2000; Wilkinson et al., 2003; Day-Stirrat et al., 2010). Thus, the ratio of targeting elements (Al, Si, Ca, and K) to immobile elements can be used to evaluate chemical changes during geological processes (Land et al., 1997; Land and Milliken, 2000; Wilkinson et al., 2003).

The changes in the element ratios with depth, a method that was put forward by Land et al. (1997), are used here to evaluate the mobility of major elements such as Al, Si, Ca, and K (Fig. 18). To acquire the statistics law of the changes in the element ratios with depth, 64 XRF data points obtained using a handheld XRF instrument are evaluated. Ti and Zr are commonly assumed to be standard immobile elements in siliciclastic geochemical systems (Land et al., 1997; Land and Milliken, 2000; Wilkinson et al., 2003). Thus, the change in element ratios Al_2O_3/Zr, Al_2O_3/TiO_2, SiO_2/Zr, SiO_2/TiO_2, K_2O/Zr, K_2O/TiO_2, CaO/Zr, and CaO/TiO_2 with burial depth are compared for samples from different depth (Fig. 18). Because of the very low solubility of aluminum, the transport of a large amount of aluminum under a subsurface condition with very low flux is impossible (Land et al., 1997; Land and Milliken, 2000; Bjørlykke, 1998; Giles, 1987; Giles and de Boer, 1990). Therefore, the Al_2O_3/Zr and Al_2O_3/TiO_2 ratios of the mudstone samples of Es3z are almost constant with increasing burial depth (Fig. 18A and B). The constant content of Al_2O_3 in the mudstone also suggests little influence from sorting/grain size. There is no correlation between Si and Al contents and the low content of feldspar (Figs. 11 and 13A), which indicate that Al is mainly hosted in clay minerals. Consistent mineralogical compositions of the mudstones are further demonstrated from the consistant total amount of clay minerals in all samples (Fig. 11).

The SiO_2/Zr ratio also shows no obvious change with increasing burial depth (Fig. 18C). However, the SiO_2/TiO_2 ratio displays a slight
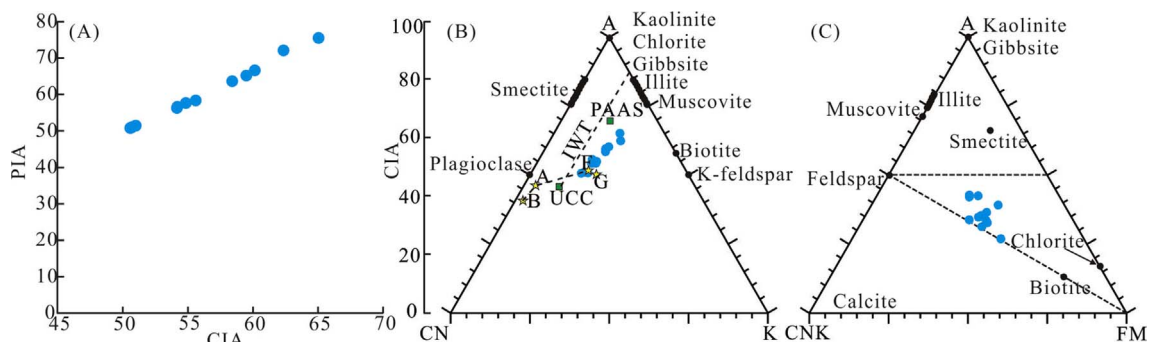

Fig. 17. The geochemical weathering trends of mudstone samples of Es3z in Dongying sag (in Appendix 2). (A) Bivariate diagram for CIA vs. PIA. (B) A-CN-K ternary diagram showing weathering trend. A = Al_2O_3; CN = $(CaO* + Na_2O)$; K = K_2O (all in molar proportions). Linked stars: B, basalt; A, andesite; F, felsic igneous rock; G, granite, represent typical primary source trend (Condie, 1993). UCC, upper continental crust; PAAS, post-Archean Australian shale (Taylor and McLennan, 1985). The ideal weathering trend (dashed line; IWT) implies a felsic source close to UCC. (C) A-CNK-FM plots (after Nesbitt et al., 1996) for the mudstone samples in the Es3z; A = Al_2O_3, CNK = $CaO* + Na_2O + K_2O$, FM = $Fe_2O_3 + MgO$ (all in molar proportions).
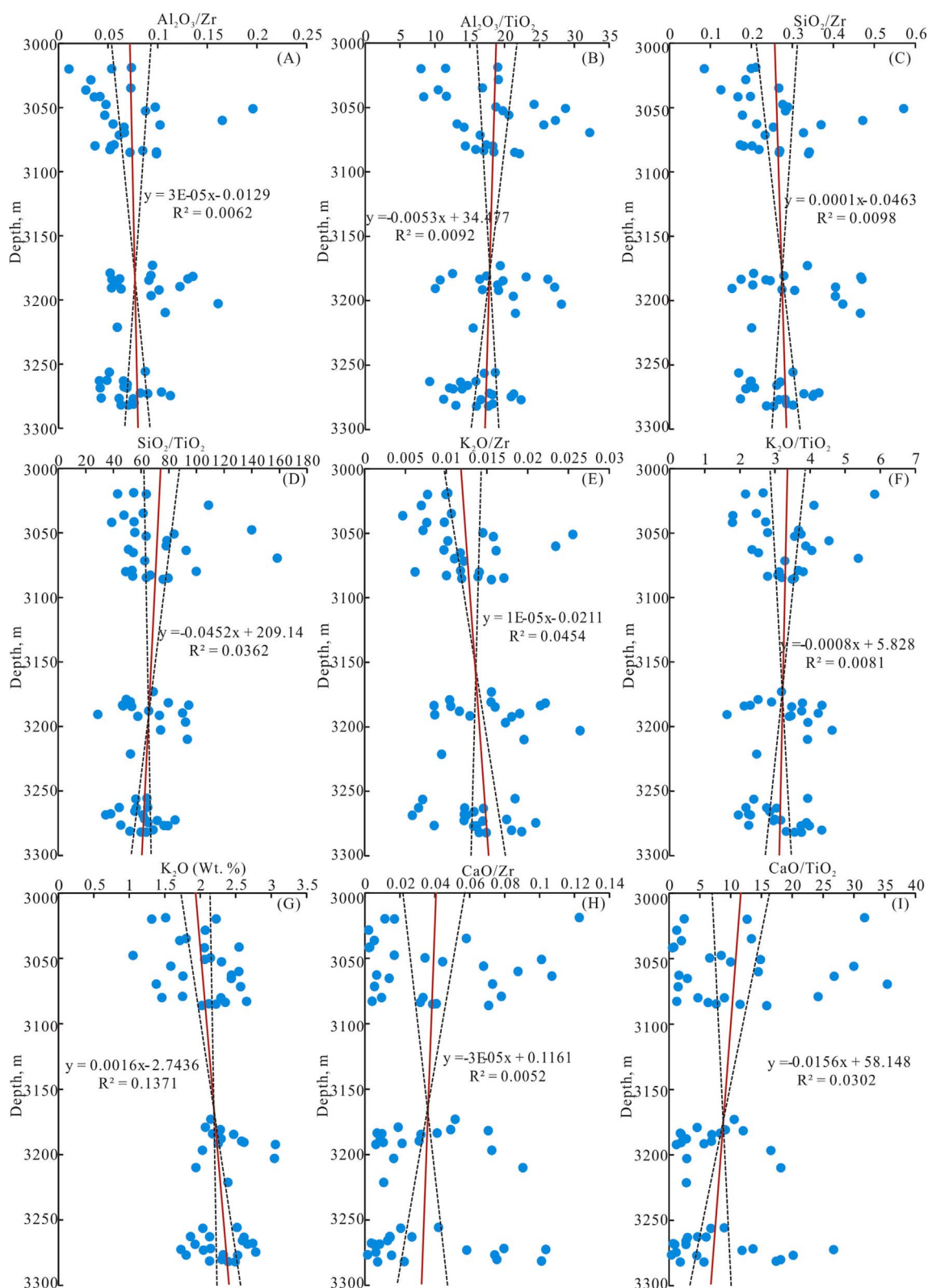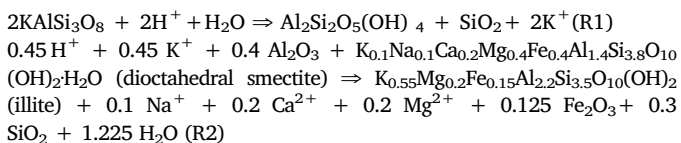
Fig. 18. Variations of the major elements ratios vs. the immobile element content in mudstones of Es3z with burial depth. In all cases, the slopes of the 95% confidence intervals (dashed lines) have the same sense as the slope of the regression line (full lines).

decrease as burial depth increases, which indicates a slight SiO_2 loss through diagenesis (Land et al., 1997; Land and Milliken, 2000; Wilkinson et al., 2003; Day-Stirrat et al., 2010). Increasing quartz-content is associated with the decreases of feldspar-content (Fig. 11). If the quartz increase occurred during deposition, the content of feldspar should increase simultaneously in the mudstone (Day-Stirrat et al., 2010). The transformation of K-feldspar to kaolinite (R1) and illite-smectite mixed layer minerals into illite (R2) is assumed to be the main process to generate silica in mudstone (Boles and Franks, 1979; McKinley et al., 2003):

$2KAlSi_3O_8 + 2H^+ + H_2O \Rightarrow Al_2Si_2O_5(OH)_4 + SiO_2 + 2K^+ (R1)$

$0.45\,H^+ + 0.45\,K^+ + 0.4\,Al_2O_3 + K_{0.1}Na_{0.1}Ca_{0.2}Mg_{0.4}Fe_{0.4}Al_{1.4}Si_{3.8}O_{10}(OH)_2 \cdot H_2O$ (dioctahedral smectite) $\Rightarrow K_{0.55}Mg_{0.2}Fe_{0.15}Al_{2.2}Si_{3.5}O_{10}(OH)_2$ (illite) $+ 0.1\,Na^+ + 0.2\,Ca^{2+} + 0.2\,Mg^{2+} + 0.125\,Fe_2O_3 + 0.3\,SiO_2 + 1.225\,H_2O$ (R2)

The content of clay minerals is steady at approximately 60 wt. % in the mudstones. The increase of illite from 30 to 60 wt. % and the decrease of K-feldspar from 4.0 to 0.5 wt. % would generate 1.2% quartz in total, which correspond to increase of the quartz content from 13.0% to 14.6% as burial depth increases (Fig. 11). Thus, we suggest that the increasing content of quartz may be caused by precipitation of silica from the transformation of K-feldspar and clay minerals (smectite transforming into illite) (Boles and Franks, 1979; McKinley et al., 2003), and was exhibited as both quartz overgrowths and microcrystalline authigenic quartz (Fig. 8D and E).

The K_2O/Zr ratio increases with depth are evident in Fig. 18E. Although the K_2O/TiO_2 ratio slightly decreases with depth (Fig. 18F), the increase of K_2O content from 1.9 to 2.4% is also obvious (Fig. 18G). Thus, the mudstones of Es3z may have gained potassium during the diagenetic evolution. The gain of components in mudstones may be difficult to explain (Awwiller, 1993; Land et al., 1997; Wilkinson et al., 2003; Geloni et al., 2015). However, taking the clay mineral transformation and decreasing content of K-feldspar into consideration, the mass imbalance clearly indicates the potassium gain in the mudstones of Es3z. The transformation from illite-smectite mixed layer minerals into illite (R2) is assumed to be the main process to consume potassium in mudstone (Boles and Franks, 1979; McKinley et al., 2003). The content of illite increases from 30 to 60 wt. % as burial depth increases (Fig. 12). According to mass balance calculation (R2), an increase of 30 wt. % illite requires 5.9 wt. % K-feldspar to supply the potassium. However, the decrease of K-feldspar from 4.0 to 0.5 Wt. % is insufficient for the compensation. Thus, other sources of potassium are required, which can be sourced from the transformation of K-feldspar to kaolinite in the adjacent sandstones (Land et al., 1997; Wilkinson et al., 2003).

The CaO/Zr and CaO/TiO_2 ratios of the mudstones of Es3z display obvious decreasing trends with increasing burial depth (Fig. 18H and I), which implies a loss of Ca during the diagenetic evolution. The lower content of CaO may due to the decrease of carbonate at deeper burial depth (Figs. 11 and 13D). Moreover, the fracture-filling calcites in the mudstones associated with oil migration also indicate that the carbonate in the mudstones may dissolve and migrate to the adjacent sandstones during the oil migration (Fig. 7F). The change of carbon and oxygen isotopic compositions of carbonates in the mudstones also indicates the possibility of a loss of Ca. The lower $\delta^{18}O$ value indicates a relative high precipitation temperature of carbonate cements, and the lower $\delta^{13}C$ value indicates an influence of organic materials during the precipitation of carbonate cements (Mansurbeg et al., 2012; Yuan et al., 2015). The correlation of carbon and oxygen isotopes and the decreasing $\delta^{13}C$ and $\delta^{18}O$ values with increasing burial depth indicate dissolution and replacement of some of the early carbonate cements (Fig. 19). The pore water carried the dissolved ions from the carbonate in the mudstone to the adjacent sandstones via both advection and diffusion (Milliken and Land, 1993; Land et al., 1997; Land and Milliken, 2000; Milliken, 2005). Moreover, the increasing content of carbonate in the adjacent sandstones from the middle of the sandstone layers to the boundary between sandstone and mudstone also supports this conclusion (Yang et al., 2017).

5.3. Implications for sandstone reservoir quality

To what extent the diagenesis of mudstones affects the diagenesis of interbedded sandstones is still controversial worldwide (Curtis, 1978; Boles and Franks, 1979; Land et al., 1997; Land and Milliken, 2000; Milliken, 2005; Gier et al., 2015). The diagenetic evolution and chemical changes of the mudstones of Es3z have a major influence on the sandstone diagenesis and reservoir quality. According to the analyzed chemical changes, aluminum and silicon seems to have re-precipitated as authigenic minerals in the mudstones (Schieber et al., 2000). Potassium has been gained by the mudstones with increasing depth, while calcium has been expelled. The mass transfer analysis from Yang et al. (2017) indicated that calcium was lost from mudstones to sandstones, and sandstone is probably the potential source of potassium for mudstone (Land et al., 1997; Gier, 1998; Wilkinson et al., 2003). Although the mechanism for potassium transport from sandstone to mudstone is not clear, the migration of potassium enhances the kaolinization of feldspar in the sandstone (Geloni et al., 2015). Since the aluminum and silicon re-precipitate as authigenic minerals in the sandstone, a small amount of secondary porosity was generated during kaolinization of feldspar (Giles, 1987; Giles and de Boer, 1990; Bjørlykke and Jahren, 2012; Taylor et al., 2010; Yuan et al., 2015). On the contrary, calcium released from mudstone to sandstone lead to the precipitation of carbonate cements that result in a decrease of primary porosity (Gier et al., 2008; Yuan et al., 2015). Thus, the mass transfer between interbedded mudstone and sandstone will decrease the reservoir quality of the sandstone. The carbonates content in mudstones may be the dominant factor affecting the sandstone reservoir quality in the Es3z in Dongying sag.
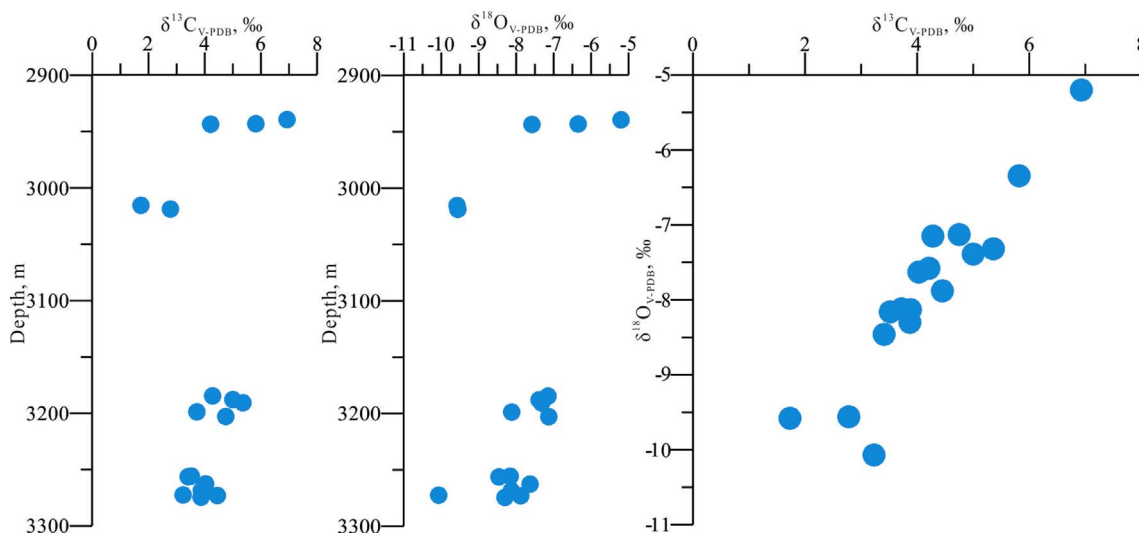

Fig. 19. C-O isotope distribution of the mudstone in the Es3z of the Dongying sag.

6. Conclusions

(1) The mineralogy of the mudstones of Es3z in Dongying sag is dominated by clay minerals (56.8%) followed by carbonates (18.2%), quartz (14.9%), feldspars (8.4%), pyrite (0.9%), anhydrite (0.8%), and TOC (2.4%).

(2) Carbonates and clay minerals are the most common cements in mudstones of Es3z. However, authigenic pyrite, albite, and quartz were occasionally observed. In the eogenetic stage, the diagenesis includes precipitation of pyrite, siderite, dolomite, calcite, and transformation of K-feldspar to kaolinite. In the mesogenetic stage, the main diagenetic events are precipitation of fracture-filling calcites, ferron calcite, ankerite, quartz overgrowths, microcrystalline authigenic quartzes and transformation of K-feldspar to illite and albite.

(3) The mudstones of Es3z in Dongying sag has felsic igneous rocks as provenance, and the source materials have endured relatively low intensity of weathering.

(4) Aluminum and silicon tend to have re-precipitated as authigenic minerals in the mudstones of Es3z, while, potassium is gained from interbedded sandstones, and calcium is lost to the sandstones.

(5) The content of carbonate in the mudstones is probably the key factor affecting the sandstone reservoir quality of Es3z in Dongying sag.

Acknowledgements

Appendix A. Supplementary data

Supplementary data related to this article can be found at http://dx.doi.org/10.1016/j.marpetgeo.2018.02.005.

References

Aagaard, P., Egeberg, P.K., Saigal, G.C., Morad, S., Bjorlykke, K., 1990. Diagenetic albitization of detrital K-feldspars in Jurassic, Lower Cretaceous, and Tertiary clastic reservoir rocks from offshore Norway, II: formation water chemistry and kinetic considerations. J. Sediment. Petrol. 60, 575–581.

Al-Aasm, I.S., Taylor, B.E., South, B., 1990. Stable isotope analysis of multiple carbonate samples using selective acid extraction. Chem. Geol. 80, 119–125.

Awwiller, D.N., 1993. Illite/smectite formation and potassium mass transfer during burial diagenesis of mudrocks: a study from the Texas gulf coast Paleocene-Eocene. J. Sediment. Petrol. 63, 501–512.

Bao, X.H., Hao, F., Fang, Y., 2007. Evolution of Geopressure Fields in the Niuzhuang Sag of the Dongying Depression and Their Effect on Petroleum Accumulation, vol. 32. Earth Science-Journal of China University of Geosciences, pp. 241–246 (in Chinese with English abstract).

Bjørlykke, K., Aagaard, P., Egeberg, P.K., Simmons, S.P., 1995. Geochemical constraints from formation water analyses from the North Sea and Gulf Coast Basin on quartz, feldspar and illite precipitation in reservoir rocks. In: In: Cubitt, J.M., England, W.A. (Eds.), The Geochemistry of Reservoirs, Geochemical Soc. Spec. Pub, vol. 86. pp. 33–50.

Bjørlykke, K., 1998. Clay mineral diagenesis in sedimentary basins — a key to the prediction of rock properties. Examples from the North Sea Basin. Clay Miner. 33, 15–34.

Bjørlykke, K., 1999. Principal Aspects of Compaction and Fluid Flow in Mudstones, Muds and Mudstone; Physical and Fluid-flow Properties, vol. 158. Geological Society of London, London, United Kingdom, pp. 73–78.

Bjørlykke, K., 2011. Open-system chemical behaviour of Wilcox Group mudstones. How is large scale mass transfer at great burial depth in sedimentary basins possible? A discussion. Mar. Petrol. Geol. 28, 1381–1382.

Bjørlykke, K., Jahren, J., 2012. Open or closed geochemical systems during diagenesis in sedimentary basins: constraints on mass transfer during diagenesis and the prediction of porosity in sandstone and carbonate reservoirs. AAPG Bull. 96, 2193–2214.

Bjørlykke, K., 2014. Relationships between depositional environments, burial history and rock properties. Some principal aspects of diagenetic process in sedimentary basins. Sediment. Geol. 301, 1–14.

Boles, J.R., Franks, S.G., 1979. Clay diagenesis in Wilcox sandstones of Southwest Texas: impolications of smectite diagenesis on sandstone cementation. J. Sediment. Petrol. 49, 55–70.

Boles, J.R., Johnson, K.S., 1983. Influence of mica surfaces on pore-water pH. Chem. Geol. 43, 303–317.

Cai, J.G., 2003. Organo-clay Complexes in Muddy Sediments and Mudstones. Tongji University, Shanghai (in Chinese with English abstract).

Cai, L.M., Chen, H.H., Li, C.Q., Li, Z.Q., Liu, H.M., Hao, X.F., 2009. Reconstruction of the Es3 palaeo-fluid potential field of in the Dongying Sag of the Jiyang Depression by systematic fluid inclusion analysis. Oil Gas Geol. 30, 19–25 (in Chinese with English abstract).

Cao, Y.C., Yuan, G.H., Li, X.Y., Wang, Y.Z., Xi, K.L., Wang, X.M., Jia, Z.Z., Yang, T., 2014. Characteristics and origin of abnormally high porosity zones in buried Palaeogene clastic reservoirs in the Shengtuo area, Dongying Sag, East China. Petrol. Sci. 11, 346–362.

Chen, D.X., Pang, X.Q., Jiang, Z.X., Zeng, J.H., Qiu, N.S., Li, M.W., 2009. Reservoir characteristics and their effects on hydrocarbon accumulation in lacustrine turbidites in the Jiyang Super-depression, Bohai Bay Basin, China. Mar. Petrol. Geol. 26, 149–162.

Claeys, P.F., Mount, J.F., 1991. Diagenetic origin of carbonate, sulfide and oxide inclusions in biotites of the great valley group (Gretaceous), Sacraento valley, California. J. Sediment. Petrol. 61, 719–731.

Condie, K.C., 1993. Chemical composition and evolution of the upper continental crust: contrasting results from surface samples and shales. Chem. Geol. 104, 1–37.

Cullers, R.L., Basu, A., Suttner, L.J., 1988. Geochemical signature of provenance in sand-size material in soils and stream sediments near the Tobacco Root batholith, Montana, USA. Chem. Geol. 70, 335–348.

Cullers, R.L., 1994. The controls on the major and trace element variation of shales, siltstones, and sandstones of Pennsylvanian-Permian age from uplifted continental blocks in Colorado to platform sediment in Kansas, USA. Geochem. Cosmochim. Acta 58, 4955–4972.

Curtis, C.D., 1978. Possible links between sandstone diagenesis and depth-related geochemical reactions occurring in enclosing mudstones. J. Geol. Soc. London 135, 107–117.

Day-Stirrat, R.J., Milliken, K.L., Dutton, S.P., Loucks, R.G., Hillier, S., Aplin, A.C., Schleicher, A.M., 2010. Open-system chemical behavior in deep wilcox group mudstones, Texas gulf coast, USA. Mar. Petrol. Geol. 27, 1804–1818.

Dickson, J.A.D., 1966. Carbonate identification and genesis as revealed by staining. J. Sediment. Petrol. 36, 491–505.

Dowey, P.J., Taylor, K.G., 2017. Extensive authigenic quartz overgrowths in the gas-bearing Haynesville-Bossier Shale, USA. Sediment. Geol. 356, 15–25.

Dutton, S.P., 2008. Calcite cement in Permian deep-water sandstones, Delaware Basin, west Texas: origin, distribution, and effect on reservoir properties. AAPG Bull. 92, 765–787.

Fedo, C.M., Wayne Nesbitt, H., Young, G.M., 1995. Unraveling the effects of potassium metasomatism in sedimentary rocks and paleosols, with implications for paleo-weathering conditions and provenance. Geology 23, 921–924.

Friedman, N., O'Neil, J.R., 1977. Compilation of stable isotope fractionation factor. In: US Geological Survey Professional Paper 440-KK.

Geloni, C., Ortenzi, A., Consonni, A., 2015. Reactive transport modelling of compacting siliciclastic sediment diagenesis. In: In: Armitage, P.J., Butcher, A.R., Churchill, J.M., Csoma, A.E., Hollis, C., Lander, R.H., Omma, J.E., Worden, R.H. (Eds.), Reservoir Quality of Clastic and Carbonate Rocks: Analysis, Modelling and Prediction, vol. 435 Geological Society London Special Publications. https://doi.org/10.1144/SP435.7.

Gier, S., 1998. Burial diagenetic process and clay mineral formation in the Molasse zone of Upper Austria. Clay Clay Miner. 46 (6), 658–669.

Gier, S., Worden, R.H., Johns, W.D., Kurzweil, H., 2008. Diagenesis and reservoir quality of Miocene sandstones in the Vienna basin, Austria. Mar. Petrol. Geol. 25, 681–695.

Gier, S., Worden, R.H., Krois, P., 2015. Comparing clay mineral diagenesis in interbedded sandstones and mudstones, Vienna Basin, Austria. In: In: Armitage, P.J., Butcher, A.R., Churchill, J.M., Csoma, A.E., Hollis, C., Lander, R.H., Omma, J.E., Worden, R.H. (Eds.), Reservoir Quality of Clastic and Carbonate Rocks: Analysis, Modelling and Prediction, vol. 435 Geological Society London Special Publications. http://doi.org/10.1144/SP435.9.

Giles, M.R., 1987. Mass transfer and problems of secondary porosity creation in deeply buried hydrocarbon reservoirs. Mar. Petrol. Geol. 4, 188–204.

Giles, M.R., de Boer, R.B., 1990. Origin and significance of redistributional secondary porosity. Mar. Petrol. Geol. 7, 378–397.

Gluyas, J., Garland, C., Oxtoby, N.H., Hogg, A.J.C., 2000. Quartz cement: the Miller's tale. In: In: Worden, R.H., Morad, S. (Eds.), Quartz Cementation in Sandstones, International Association of Sedimentology, vol. 29. pp. 199–218 Special Publication.

Guo, J., Zeng, J.H., Song, G.Q., Zhang, Y.W., Wang, X.J., Meng, W., 2014. Characteristics and Origin of Carbonate Cements in the Shahejie Formation of the Central Uplift Belt in the Dongying Depression, vol. 39. Earth Science-Journal of China University of

Geoscience, pp. 565–576 (in Chinese with English abstract).

Han, Y.J., He, S., Song, G.Q., Wang, Y.S., Hao, X.F., Wang, B.J., Luo, S.Y., 2012. Origin of carbonate cements in the overpressured top seal and adjacent sandstones in Dongying depression. Acta Pet. Sin. 33, 385–393 (in Chinese with English abstract).

Hao, Y.Q., Chen, F.K., Zhu, J.Q., Zhang, S.P., 2014. Reservoir space of the Es33-Es41 shale in Dongying sag. Int. J. Min. Sci. Technol. 24, 425–431.

He, S., Song, G.Q., Wang, Y.S., Hao, X.F., Wang, B.J., Li, N., Luo, S.Y., 2012. Distribution and Major Control Factors of the Present-day Large-scale Overpressured System in Dongying Depression, vol. 37. Earth Science-Journal of China University of Geoscience, pp. 1029–1104 (in Chinese with English abstract).

Hillier, S., 2003. Quantitative analysis of clay and other minerals in sandstones by X-ray powder diffraction (XRPD). In: In: Worden, R.H., Morad, S. (Eds.), Clay Mineral Cements in Sandstones. International Association of Sedimentologists Special Publication, vol. 34. Blackwell Science, pp. 213–251.

Kasi, A.K., Kassi, A.M., Friis, H., Umar, M., Mohibullah, M., Kakar, M.I., 2016. Detrital mode and whole-rock geochemistry of the Miocene-Pliocene fluvial succession, Pishin Belt, Pakistan: implications on provenance and source area weathering in peripheral foreland basins. Arabian J. Geosci. 9, 1–21.

Land, L.S., Mack, L.E., Milliken, K.L., Leo Lynch, F., 1997. Burial diagenesis of argillaceous sediment, south Texas Gulf of Mexico sedimentary basin: a reexamination. GSA Bull. 109, 2–15.

Land, L.S., Milliken, K.L., 2000. Regional loss of SiO2 and CaCO3, and gain of K2O during burial diagenesis of Gulf Coast mudrocks, U.S.A. In: In: Worden, R.H., Morad, S. (Eds.), Quartz Cementation in Sandstones. International Association of Sedimentologists, vol. 29. pp. 183–197 Special Publication.

Liang, C., Jiang, Z., Zhang, C., Guo, L., Yang, Y., Li, J., 2014. The shale characteristics and shale gas exploration prospects of the Lower Silurian Longmaxi shale, Sichuan Basin, South China. J. Nat. Gas Sci. Eng. 21, 636–648.

Liu, C.L., Zhao, Q.H., Wang, P.X., 2002. Water chemistry of the Paleogene Dongying lake: evidence from fossil assemblages and shell isotopes. Acta Geosci. Sin. 23, 237–242 (in Chinese with English abstract).

Macquaker, J.H.S., Taylor, K.G., Keller, M., Polya, D., 2014. Compositional controls on early diagenetic pathways in fine-grained sedimentary rocks: Implications for predicting unconventional reservoir attributes of mudstones. AAPG Bull. 98, 587–603.

Mansurbeg, H., De Ros, L.F., Morad, S., Ketzer, J.M., El-Ghali, M.A.K., Caja, M.A., Othman, R., 2012. Meteoric-water diagenesis in late Cretaceous canyon-fill turbidite reservoirs from the Espírito Santo Basin, eastern Brazil. Mar. Petrol. Geol. 37, 7–26.

McAllister, R.T., Taylor, K., Garcia-Fresca, B., Hollis, C., 2015. Diagenetic Evolution of the Eagle Ford Formation, SW Texas: Impacts upon Reservoir Quality and Rock Properties. pp. 1–12.

McKinley, J.M., Worden, R.H., Ruffell, A.H., Worden, R.H., Morad, S., 2003. Smectite in sandstones: a review of the controls on occurrence and behaviour during diagenesis. In: Clay Mineral Cement in Sandstones, vol. 34. International Association of Sedimentologists, pp. 109–128 Special Publication.

McLennan, S.M., Hemming, S., McDaniel, D.K., Hanson, G.N., 1993. Geochemical approaches to sedimentation, provenance, and tectonics. Geol. Soc. Am. Spec. Pap. 284, 21–40.

Milliken, K.L., Land, L.S., 1993. The origin and fate of silt sized carbonate in subsurface Miocene-Oligocene mudstones, south Texas Gulf Coast. Sedimentology 40, 107–124.

Milliken, K.L., Mack, L.E., Land, L.S., 1994. Elemental mobility in sandstones during burial: whole-rock chemical and isotopic data, Frio Formation, South Texas. J. Sediment. Res. 64, 788–796.

Milliken, K.L., 2005. Late diagenesis and mass transfer in sandstone-shale sequences. In: Mackenzie, F.T. (Ed.), Treatise on Geochemistry 7: Sediments, Diagenesis and Sedimentary Rocks.

Milliken, K.L., Esch, W.L., Reed, R.M., Zhang, T., 2012. Grain assemblages and strong diagenetic overprinting in siliceous mudrocks, Barnett Shale (Mississippian), Fort Worth Basin, Texas. AAPG Bull. 96, 1553–1578.

Milliken, K.L., Day-Stirrat, R., 2013. Cementation in mudrocks: Brief review with examples from cratonic basin mudrocks. In: In: Chatellier, J.Y., Jarvie, D.M. (Eds.), Critical Assessment of Shale Resource Plays: AAPG Memoir, vol. 103. pp. 133–160.

Milliken, K.L., 2014. A Compositional Classification For Grain Assemblages In Fine-Grained Sediments and Sedimentary Rocks. J. Sediment. Res. 84, 1185–1199.

Milliken, K.L., Ergene, S.M., Ozkan, A., 2016. Quartz types, authigenic and detrital, in the Upper Cretaceous Eagle For Formation, South Texas, USA. Sediment. Geol. 339, 273–288.

Milliken, K.L., Shen, Y., Ko, L.T., Liang, Q.S., 2017. Grain composition and diagenesis of organic-rich lacustrine tarls, Triassic Yanchang Formation, Ordos Basin, China. Interpretation 5, 189–210.

Moore, D.M., Reynolds Jr., R.C., 1997. X-Ray Diffraction and the Identification and Analysis of Clay Minerals, second ed. Oxford Univ. Press, Oxford, pp. 378.

Mortimer, R.J.G., Coleman, M.L., 1997. Microbial influence on the oxygen isotopic composition of diagenetic siderite. Geochem. Cosmochim. Acta 61, 1705–1711.

Nesbitt, H.W., Young, G.M., 1982. Early Proterozoic climates and plate motions inferred from major element chemistry of lutites. Nature 299, 715–717.

Nesbitt, H.W., Young, G.M., McLennan, S.M., Keays, R.R., 1996. Effects of chemical weathering and sorting on the petrogenesis of siliciclastic sediments, with implications for provenance studies. J. Geol. 104, 525–542.

Peltonen, C., Marcussen, Ø., Bjørlykke, K., Jahren, J., 2009. Clay mineral diagenesis and quartz cementation in mudstones: The effects of smectite to illite reaction on rock properties. Mar. Petrol. Geol. 26, 887–898.

Preston, J., Hartley, A., Hole, M., Buck, S., Bond, J., Mange, M., Still, J., 1998. Integrated whole-rock trace element geochemistry and heavy mineral chemistry studies: aids to the correlation of continental red-bed reservoirs in the Beryl Field, UK North Sea. Petrol. Geosci. 4, 7–16.

Robinson, P., 2003. XRF analysis of flux-fused discs. In: 5th International Conference on the Analysis of Geological and Environmental Materials, vol. 90 Abstracts.

Şans, B.E., Esenli, F., Kadir, S., Elliott, W.C., 2015. Genesis of smectite in siliciclastics and pyroclastics of the Eocene İslambeyli formation in the Lalapaşa region, NW Thrace, Turkey. Clay Miner. 50, 459–483.

Schieber, J., Krinsley, D., Riciputi, L., 2000. Diahenetic origin of quartz silt in mudstones and implications for silica cycling. Nature 406, 981–985.

Shaw, H.F., Conybeare, D.M., 2003. Patterns of clay mineral diagenesis in interbedded mudrocks and sandstones: an example from the Palaeocene of the North Sea. In: In: Worden, R.H., Morad, S. (Eds.), Clay Mineral Cement in Sandstones, vol. 34. International Association of Sedimentologists, pp. 129–145 Special Publication.

Su, J.B., Zhu, W.B., Lu, H.F., Xu, M.J., Yang, W., Zhang, Z.Y., 2009. Geometry styles and quantification of inversion structures in the Jiyang depression, Bohai Bay Basin, eastern China. Mar. Petrol. Geol. 26, 25–38.

Sui, F.G., Liu, Q., Zhang, L.Y., 2007. Diagenetic evolution of source rocks and its significance to hydrocarbon expulsion in Shahejie formation of Jiyang depression. Acta Pet. Sin. 28, 12–16 (in Chinese with English abstract).

Svendsen, J.B., Hartley, N.R., 2002. Synthetic heavy minerals stratigraphy: applications and limitations. Mar. Petrol. Geol. 19, 389–405.

Taylor, S.R., McLennan, S.M., 1985. The Continental Crust: its Composition and Evolution. Blackwell, Oxford.

Taylor, K.G., Macquaker, J.H.S., 2000. Early diagenetic pyrite morphology in a mudstone-dominated succession: the Lower Jurassic Cleveland Ironstone Formation, eastern England. Sediment. Geol. 131, 77–86.

Taylor, T.R., Giles, M.R., Hathon, L.A., Diggs, T.N., Braunsdorf, N.R., Birbiglia, G.V., Kittridge, M.G., Macaulay, C.I., Espejo, I.S., 2010. Sandstone diagenesis and reservoir quality prediction: models, myths, and reality. AAPG Bull. 94, 1093–1132.

Taylor, K.G., Macquaker, J.H.S., 2014. Diagenetic alterations in a silt- and clay-rich mudstone succession: an example from the Upper Cretaceous Mancos Shale of Utah, USA. Clay Miner. 49, 213–227.

Thyberg, B., Jahren, J., 2011. Quartz cementation in mudstones: sheet-like quartz cement from clay mineral reactions during burial. Petrol. Geosci. 17, 53–63.

Vosoughi Moradi, A., Sarı, A., Akkaya, P., 2016. Geochemistry of the Miocene oil shale (Hançili Formation) in the Çankırı-Çorum Basin, Central Turkey: Implications for Paleoclimate conditions, source–area weathering, provenance and tectonic setting. Sediment. Geol. 341, 289–303.

Wang, W.Q., Zhang, S.P., Xie, Z.H., Liu, Y., 2008. Discussion on the relationship between hydrocarbon-traced diagenetic minerals and reservoirs formation: case study in Dongying Depression. PGRE 15, 14–17 (in Chinese with English abstract).

Wang, J.D., Li, S.Z., Santosh, M., Dai, L.M., Suo, Y.H., Yu, S., Zhao, S.J., Liu, B., Wang, Q.J., 2013. Lacustrine turbidites in the Eocene Shahejie Formation, Dongying Sag, Bohai Bay Basin, North China Craton. Geol. J. 48, 561–578.

Wang, Y.Z., Cao, Y.C., Ma, B.B., Liu, H.M., Gao, Y.J., Chen, L., 2014. Mechanism of diagenetic trap formation in nearshore subaqueous fans on steep rift lacustrine basin slopes-A case study from the Shahejie Formation on the north slope of the Minfeng Subsag, Bohai Bay Basin, China. Petrol. Sci. 11, 481–494.

Wilkinson, M., Haszeldine, R.S., Milliken, K.L., 2003. Cross formational flux of aluminium and potassium in Gulf Coast sediments. In: In: Worden, R., Morad, S. (Eds.), Clay Cements in Sandstones, vol. 34. International Association of Sedimentologists, pp. 147–160 Special Publication.

Worden, R.H., Morad, S., 2000. Quartz cementation in oil field sandstones: a review of the key controversies. In: In: Worden, R.H., Morad, S. (Eds.), Quartz Cementation in Sandstones. International Association of Sedimentologists, vol. 26. pp. 1–20 Special Publication.

Yang, T., Cao, Y.C., Wang, Y.Z., Li, Y., Zhao, S.M., 2015. Status of and trends in research on deep- water gravity flow deposits. Acta Geol. Sin (English Edition) 89, 801–822.

Yang, T., Cao, Y.C., Wang, Y.Z., Friss, H., Haile, B.G., Xi, K.L., Zhang, H.N., 2016. The coupling of dynamics and permeability in the hydrocarbon accumulation period controls the oil-bearing potential of low permeability reservoirs: a case study of the low permeability turbidite reservoirs in the middle part of the third member of Shahejie Formation in Dongying Sag. Petrol. Sci. 13, 204–224.

Yang, T., Cao, Y.C., Friis, H., Liu, K.Y., Wang, Y.Z., Zhou, L.L., Zhang, S.M., Zhang, H.N., 2017. Genesis and distribution pattern of carbonate cements in lacustrine deep-water gravity-flow sandstone reservoirs in the third member of the Shahejie Formation in the Dongying Sag, Jiyang Depression, Eastern China. Mar. Petrol. Geol (in press). https://doi.org/10.1016/j.marpetgeo.2017.11.020.

Yuan, G., Gluyas, J., Cao, Y., Oxtoby, N.H., Jia, Z., Wang, Y., Xi, K., Li, X., 2015. Diagenesis and reservoir quality evolution of the Eocene sandstones in the northern Dongying Sag, Bohai Bay Basin, East China. Mar. Petrol. Geol. 62, 77–89.

Zhang, C.L., Horita, J., Cole, D.R., Zhou, J.Z., Lovley, D.R., Phelps, T., 2001. Temperature-dependent oxygen and carbon isotope fractionations of biogenic siderite. Geochem. Cosmochim. Acta 65, 2257–2271.

Zhang, L.Y., Liu, Q., Zhu, R.F., Li, Z., Lu, X.C., 2009. Source rocks in Mesozoic–Cenozoic continental rift basins, east China: A case from Dongying Depression, Bohai Bay Basin. Org. Geochem. 40, 229–242.

Zhang, Q., Zhu, X.M., Steel, R.J., Zhong, D.K., 2014. Variation and mechanisms of clastic reservoir quality in the Palaeogene Shahejie Formation of the Dongying Sag, Bohai Bay Basin, China. Petrol. Sci. 11, 200–210.

Zhou, L., Friis, H., Poulsen, M.L.K., 2015. Geochemical evaluation of the Late Paleocene and Early Eocene shales in Siri Canyon, Danish-Norwegian Basin. Mar. Petrol. Geol. 61, 111–122.

Zhu, G.H., Zhang, J., Yao, G.S., Li, Y.W., Wang, X., Yu, C.F., 2014. Sedimentary volcanic dust tuff, An important kind of rock storing hydrocarbon resources: disscusion on the lithology of middle permian lucaogou oil-bearing rocks in the north of Xinjiang. Marine Origin Petrol. Geol. 19, 1–7 (in Chinese with English abstract).